UNIVERSIDADE DO ESTADO DE SANTA CATARINA – UDESC
CENTRO DE CIÊNCIAS TECNOLÓGICAS – CCT
PROGRAMA DE PÓS-GRADUAÇÃO EM ENGENHARIA MECÂNICA – PPGEM

LEONARDO DEMMER KNIPPENBERG

SIMULATION OF A SINGLE-PHASE TURBULENT JET USING THE LATTICE BOLTZMANN METHOD

JOINVILLE
2025

LEONARDO DEMMER KNIPPENBERG

SIMULATION OF A SINGLE-PHASE TURBULENT JET USING THE LATTICE BOLTZMANN METHOD

Dissertação apresentada ao Programa de Pós-Graduação em Engenharia Mecânica, do Centro de Ciências Tecnológicas da Universidade do Estado de Santa Catarina, como requisito parcial para a obtenção do grau de Mestre em Engenharia Mecânica, área de concentração em Modelamento e Simulação Numérica.

Supervisor: Prof. Dr. Luiz Adolfo Hegele Júnior

JOINVILLE
2025

Ficha catalográfica elaborada pelo programa de geração automática da Biblioteca Universitária Udesc,
com os dados fornecidos pelo(a) autor(a)

Knippenberg, Leonardo
SIMULATION OF A SINGLE-PHASE TURBULENT JET USING THE LATTICE BOLTZMANN METHOD / Leonardo Knippenberg. -- 2025.
75 p.

Orientador: Luiz Adolfo Hegele Jr
Dissertação (mestrado) -- Universidade do Estado de Santa Catarina, Centro de Ciências Tecnológicas, Programa de Pós-Graduação em Engenharia Mecânica, Joinville, 2025.

1. Lattice Boltzmann method (LBM);. 2. Turbulent Jet. 3. Computational Fluid Dynamics (CFD). I. Adolfo Hegele Jr, Luiz. II. Universidade do Estado de Santa Catarina, Centro de Ciências Tecnológicas, Programa de Pós-Graduação em Engenharia Mecânica. III. Título.

LEONARDO DEMMER KNIPPENBERG

SIMULATION OF A SINGLE-PHASE TURBULENT JET USING THE LATTICE BOLTZMANN METHOD

Dissertação apresentada ao Programa de Pós-Graduação em Engenharia Mecânica, do Centro de Ciências Tecnológicas da Universidade do Estado de Santa Catarina, como requisito parcial para a obtenção do grau de Mestre em Engenharia Mecânica, área de concentração em Modelamento e Simulação Numérica.

BANCA EXAMINADORA:

Prof. Dr. Luiz Adolfo Hegele Júnior
Universidade do Estado de Santa Catarina

Membros:

Prof. Dr. Juan Pablo de Lima Costa Salazar
Universidade Federal de Santa Catarina

Prof. Dr. Leonardo Romero Monteiro
Universidade do Estado de Santa Catarina

Joinville, 28 de Janeiro de 2025

ACKNOWLEDGEMENTS

Agradeço a Deus e a minha família em especial ao meu pai Edson e minha mãe Sandra por todo o apoio durante a minha graduação e pós-graduação e ao meu irmão Guilherme.

Agradeço a minha noiva Lisania por toda a ajuda e por ser uma pessoa incrível que me inspirou a evoluir sempre.

Agradeço ao professor Dr. Luiz Adolfo Hegele Jr. pela orientação e por todas as oportunidade que me ofereceu.

Agradeço ao Geoenergia Lab por toda a ajuda durante o desenvolvimento do trabalho realizado em especial para o Vinícius Czarnobay e ao Gustavo Choaire.

Agradeço a Petrobrás pelo financiamento e oportunidade de pesquisa que possibilitou concretizar o desenvolvimento deste trabalho e demais trabalhos realizados anteriormente.

Agradeço a Universidade do Estado de Santa Catarina (UDESC) em especial o campus de Balneário Camboriú (CESFI) por todo o auxílio durante o desenvolvimento do trabalho e ao campus de Joinville (CCT) pela oportunidade da pós-graduação.

ABSTRACT

I present an approach to modeling a turbulent single-phase jet and the boundary conditions of the flow using the Lattice Boltzmann Method (LBM). The method employs a regularized version of the Boltzmann equation that incorporates a formulation for the BGK collision operator. The reconstruction of regularized particle populations is based on fourth-order moments of the distribution function based on the application of Hermite polynomials. Based on the work of (Hegele.Jr *et al.* 2018), our approach reconstructs unknown moments by means of known particle populations on the boundaries of the boundary conditions, leading to a system of equations solved according to the method. The three-dimensional mesh D3Q19 and D3Q27 is considered for the solution of the jet flow as a reference test. Comparison with literature solutions shows agreement, validating the effectiveness of the proposed method. The high-order model is tested for a flow with $Re = 2000$ in a periodic domain for the faces parallel to the fluid flow. The lattice Boltzmann method allows simulations of stable flows with low viscosity levels, which makes it possible to obtain a high Re. The proposed model makes it possible to carry out a high-performance simulation to test the processing capacity of a GPU and obtain accurate results in a relatively short period of time compared to other methods for simulating the flow of a fluid. The mesh used for the simulation has [256, 1028, 256] grid points in [x, y, z] for a Cartesian coordinate system, resulting in a total of 6.7×10^7 calculations performed per time step over a period of 9000 seconds, which results in a total of 7485 operations per second. Finally, the results obtained show compatibility with the experimental results and it is possible to confirm that the bechmark performed has a high level of processing while maintaining accuracy.

Keywords: Lattice Boltzmann method (LBM); Turbulent Jet; Computational Fluid Dynamics (CFD).

RESUMO

Apresento uma abordagem para modelar um jato monofásico turbulento e as condições de contorno do escoamento utilizando o método do Lattice Boltzmann (LBM). O método emprega uma versão regularizada da equação de Boltzmann que incorpora uma formulação para o operador de colisão BGK. A reconstrução de populações de partículas regularizadas é baseada em momentos de quarta ordem da função de distribuição com base na aplicação dos polinômios de Hermite. Baseado no trabalho de Hegele et al. (Phys. Rev. E 98, 043302, 2018), nossa abordagem reconstrói momentos desconhecidos por meio de populações de partículas conhecidas nos limites das condições de contorno, levando a um sistema de equações resolvidas de acordo com o método. A malha tridimensional D3Q19 e D3Q27 é considerado para a solução do fluxo do jato como um teste de referência. A comparação com soluções da literatura demonstra concordância, validando a eficácia do método proposto. O modelo de alta ordem é testado para um escoamento com *Re* = 2000 em um domínio periódico para as faces paralelas ao escoamento do fluido . O método lattice Boltzmann permite a realização de simulações de escoamentos estáveis com baixos níveis de viscosidade, o que possibilita a obtenção de um *Re* alto. O modelo proposto permite a realização de uma simulação de alto desempenho para testar a capacidade de processamento de uma GPU e obter resultados precisos em um período de tempo relativamente curto em comparação com outros métodos de simulação de escoamento de um fluido. A malha usada para a simulação tem [256, 1028, 256] pontos de rede em [x, y, z] para um sistema de coordenadas cartesianas, resultando em um total de 6,7 x 10^7 cálculos realizados por etapa de tempo em um período de 9000 segundos, o que resulta em um total de 7485 operações por segundo. Por fim, os resultados obtidos mostram compatibilidade com os resultados experimentais e é possível confirmar que o bechmark realizado tem um alto nível de processamento, mantendo a precisão.

Palavras-chave: Método Lattice Boltzmann (LBM); Jato Turbulento; Dinâmica de Fluidos Computacional (CFD)

LIST OF FIGURES

LIST OF ABBREVIATIONS AND ACRONYMS

BGK	Bhatnagar-Gross-Krook
CFD	Computational Fluid Dynamics
DdQq	d-Dimensional set of q-velocities
GPU	Graphics Processing Unit
IRBC	Incompressible regularization-based boundary condition
LBM	Lattice Boltzmann Method
NSE	Navier-Stokes Equations
RBC	Regularization-based boundary condition

LIST OF SYMBOLS

a_s	scaling factor
b_{jet}	shear layer of the velocity profile
B	back
B	decay rate
$\mathbf{c}_i$	particle velocity
c_s	speed of sound
E	east
E_c	kinetic energy
F	front
F	intermolecular forces
f_i	discrete-particle distribution
$f_i^{(1)}$	first-order distribution function
$f_i^{(eq)}$	equilibrium particle distribution function
$f_i^{(neq)}$	non-equilibrium particle distribution function
$\hat{f}_i$	regularized particle distribution function
$\hat{f}_i^{(neq)}$	regularized non-equilibrium particle distribution function
g	gravitational acceleration vector
$\mathscr{H}_i^{(0)}$	zero order velocity expansion in the Hermite polynomials
$\mathscr{H}_{\alpha,i}^{(1)}$	first-order velocity expansion in the Hermite polynomials
$\mathscr{H}_{\alpha\beta,i}^{(2)}$	second-order velocity expansion in the Hermite polynomials
I_s	incoming velocity set
Kn	Knudsen number
L	characteristic length
ℓ	mean free pass
$m_{\alpha\beta}^{(2)}$	second order moments
Ma	Mach number
N	north
O_s	outgoing velocity set
$\mathbf{r}$	particle position vector
Re	Reynolds Number

S	south
$S_{\alpha\beta}$	strain rate tensor
t	time
U_{exit}	inlet velocity
U_J	jet velocity
U_{max}	maximum velocity
U_s	velocity of the sound
u_α	velocity
u_l	characteristic velocity
w	weights
W	west
	Greeks
Δ_t	lattice time-step; time variation
$\delta_{\alpha,\beta}$	Kronecker delta
η	Kolmogorov scale
ν	kinematic viscosity
ω	inverse of viscosity
Ω	BGK operator
Π	strain rate tensor
ρ	specific mass or absolute density
ρ_I	zero-order moment of incoming set
τ	relaxation time
ξ	microscopic velocity

CONTENTS

1 INTRODUCTION

The study of single-phase axisymmetric turbulent jets is fundamental in various engineering applications, such as combustion, propulsion and oil industry processes. In this type of flow, a jet of fluid is expelled from a circular nozzle into a theoretically infinite environment. In addition to being common in industrial contexts, this scenario is widely studied due to its relevance to mixing phenomena, mass and energy transportation, and contaminant dispersion (Lipari e Stansby 2011).

Although extensive research has been carried out, both through experiments and numerical simulations, certain aspects remain challenging. These include turbulent behavior on microscopic scales and the statistics of high-order moments, which are fundamental to achieving greater physical fidelity and accuracy in comparing methods. Modeling turbulence at the microscale, as well as the statistical description for higher moments, requires the development of robust numerical techniques and detailed experiments (Li *et al.* 2023).

In an axisymmetric single-phase jet, the fluid consists of a single phase, such as a gas or liquid. Axisymmetry implies that the flow has rotational symmetry around a main axis, a common characteristic of jets emerging from circular orifices. The turbulence intrinsic to these flows is dominated by three-dimensional, chaotic velocity fluctuations, which manifest themselves on a wide range of spatial and temporal scales. These fluctuations play a critical role in mixing dynamics and the transport of mass, momentum and energy (Shekhar e Nishino 2019).

The mathematical description of axisymmetric single-phase turbulent jets is generally based on the Navier-Stokes equations, which govern the behavior of Newtonian fluids. The detailed analysis of these flows contributes not only to the optimization of industrial processes, but also to the mitigation of environmental impacts, such as the controlled dispersion of gaseous and liquid effluents.With advances in numerical techniques, it has become possible to gain a more detailed understanding of the turbulent structure and mixing mechanisms in these systems (Pope 2013).

Historical experimental results have played a crucial role in this field. Methods such as hot-wire anemometry and laser-Doppler velocimetry have been widely used to obtain average velocity profiles and second- and third-order velocity moments. For example, the studies by (Wygnanski e Fiedler 1969) provided an initial basis on axisymmetric isothermal jets, while (Hussein *et al.* 1994) presented contributions that remain as references for validating numerical simulations. These results are widely used by the scientific community to compare different models and computational techniques.

In this work, a computational simulation based on the Lattice Boltzmann Method (LBM) was developed to model and simulate a single-phase jet in a rectangular mesh domain. Periodic boundary conditions were applied into the radial walls to the boundaries of the computational domain, allowing repetitive or cyclic behavior to be simplified, and extending the domain to represent an infinite environment.This approach is widely used in problems where interaction with the boundaries is negligible, as highlighted in recent work by (Montessori *et al.* 2024; Ferrari e Franco 2024) and (Chen *et al.* 2020).

The experimental results available for Reynolds numbers up to $Re \equiv u_L L/\nu = 10^3$ where u_L, L and ν represent the characteristic velocity, characteristic length and viscosity of the fluid, respectively, have been widely used to validate computational methods over the last 30 years.Studies such as those by (Prasad e Koseff 1989) and (Hegele.Jr *et al.* 2018) are examples of work that consolidated experimental reliability as the basis for numerical advances.

In this study, we present a simulation scheme that allows high accuracy for simulating turbulent fluids.Using a regularized form for the distribution function $\hat{f}_i$ with fourth-order accuracy, we guarantee greater stability even for high values of Re. The proposed technique, based on the D3Q19 and D3Q27 lattice system where “D” is the number of dimensions and “Q” is the number of populations , has yet to be fully developed in the literature, especially for periodic boundary conditions applied to turbulent jets. Works such as those by (Hegele.Jr *et al.* 2018) and (Kruger 2016) have demonstrated the effectiveness of regularized functions, but have not fully explored the behaviour of turbulent jets in similar configurations.

This work seeks to fill this gap by detailing the simulation methodology, including the technical aspects of the chosen system, the collision and propagation stages, and the use of regularized distribution functions with second-order accuracy. Finally, the results obtained will be presented and the implications of using periodic boundary conditions in turbulent jet simulations will be discussed, with a focus on the physical fidelity and practical applicability of the method validated by the literature and experimental results.

1.1 OBJECTIVES

The aim of this work is to develop and implement a numerical simulation of an axisymmetric turbulent jet using the Lattice Boltzmann Method, with a focus on analyzing and improving the boundary conditions applied to the computational domain. The proposal aims to investigate how different techniques for imposing boundary conditions affect the stability, accuracy and physical representativeness of the numerical solution, especially considering the jet inlet conditions, free boundaries and treatment of the domain outlet. The study aims to contribute to the refinement of models that use LBM in turbulent jet simulations, ensuring greater reliability in practical applications of fluid dynamics in complex geometries.

Specific Objectives

- Implement the Lattice Boltzmann Method (LBM) to simulate the flow of an axisymmetric turbulent jet in a discrete computational domain, using appropriate stencils such as D3Q19 and D3Q27.
- Validate the results obtained with known data available in the literature for similar flows, ensuring the reliability of the numerical model developed.

- Suggest improvements to the boundary conditions applied to the Lattice Boltzmann method in turbulent jet simulations, seeking solutions that offer greater physical accuracy and numerical robustness for future applications.

1.2 JUSTIFICATION

The study of turbulent jets has great relevance in various areas of engineering and science, including propulsion systems, ventilation, mixing processes in chemical reactors and the dispersion of pollutants in open environments. The correct modeling of the phenomena associated with turbulent flow is fundamental for the advancement of technologies that involve fluid dynamics and require high efficiency and precise control of processes.

Turbulence, due to its chaotic and three-dimensional nature, is one of the most challenging phenomena to describe using analytical or empirical methods. In this context, numerical simulations have emerged as a powerful tool for understanding the behavior of turbulent flows in different scenarios. Among the numerical methods available, the Lattice Boltzmann Method (LBM) is an innovative and promising alternative. Its approach based on particle distribution functions makes it possible to describe the transport of mass, quantity of movement and energy in an efficient and flexible way, with advantages in terms of parallelization and simplicity in the implementation of complex geometry.

In this work, the choice of the second-order LBM is justified by its ability to capture the effects of turbulence with greater precision, while maintaining a relatively low computational cost. In addition, the LBM allows for a better representation of medium and small scale phenomena, such as the formation of vortices and the transition between different flow regimes, essential aspects for understanding the behavior of turbulent jets.

Given the growing interest in applications involving the control and optimization of turbulent flows, this study contributes to the advancement of scientific knowledge in the area of computational fluid dynamics (CFD). The use of modern numerical methods, such as LBM, allows the frontier of knowledge to be expanded, providing more robust models that are applicable to real situations, such as predicting the performance of fuel injection systems and the dispersion of atmospheric emissions.

The work serves as validation for the method developed by (Hegele.Jr *et al.* 2018) in an applied way. The application of this simulation will serve as a reference and future developments in the area of oil spill containment, where the method used for a single-phase jet will be used to simulate the mechanical dispersion of oil droplets in a spill after the projection of a jet perpendicular to the spill as demonstrated by (Brandvik *et al.* 2023) through experimental methodologies.

1.3 TEXT STRUCTURE

The introduction was presented in Chapter 1, which provides the context, a summary of the bibliography, the objectives and the justification for the study, while Chapter 2 covers the essential concepts related to the topic. The content includes the main hydrodynamic fundamentals that will be taken into account during the development of the work, the concepts that gave rise to the Boltzmann lattice method will be presented, which are necessary for understanding the methodology used and, finally, a bibliographical review of the works related to the topic.

Chapter 3 details the methodology applied for the proposed simulation, presenting the foundations, mathematical and physical development for the conservation of mass and momentum that were applied.In Chapter 4 the results are presented, showing a comparison with experimental results governing turbulent behavior for an axisymmetric jet

Chapter 5 gives the conclusions, highlighting the main results.

2 THEORETICAL BASIS AND LITERATURE REVIEW

This chapter covers the fundamental issues for the proposed study. Firstly, the theoretical bases that directly or indirectly affect the properties of a turbulent jet flow are discussed. Next, we explore the work that has been done to describe the behavior of single-phase turbulent jets, with emphasis on numerical modeling with experimental validation.

2.1 BASICS OF HYDRODYNAMICS AND KINETIC THEORY

2.1.1 Navier-Stokes Equations

The phenomena occurring in the flow of a single-phase or multiphase fluid are described by the Navier-Stokes differential equations. When the flow is incompressible, the movement of the fluid is described by the conservation of mass and momentum, which are represented in Eq.1 and Eq.2 respectively.

$$\frac{\partial \rho \mathbf{u}}{\partial t} + \nabla \cdot (\rho \mathbf{u}) = 0, \tag{1}$$

$$\frac{\partial \rho \mathbf{u}}{\partial t} + \nabla \cdot (\rho \mathbf{u}\mathbf{u}) = \nabla \cdot \Pi + \rho \mathbf{g}, \tag{2}$$

where ρ represents the density of the fluid, $\mathbf{u}$ refers to the velocity component in a given direction, Π the stress tensor, g the resultant acceleration due to gravity and t is the time (Anderson *et al.* 1998; Jamet 2001).

For laminar flow, there are analytical solutions that describe the behavior of the fluid, but these do not solve the problem when the flow is turbulent. For this reason, the study of turbulent flows has basically been limited to experimental analysis and numerical simulations. This simulation consists of solving the Navier-Stokes equations on all turbulence scales where all the approximations made are numerical in nature. The advantage of this type of analysis is that it allows the flow to be examined in the field of space and time, but it requires a elevated computational cost.

2.1.2 Reynolds Number

The Reynolds number proposed by Osborne Reynolds (1842-1912) through experimental methods aims to differentiate the existence of two types of flow. Through flow visualization techniques, the Reynolds discovered that the flow regime of a flow depends mainly on the ratio between the inertial forces and viscous forces of a fluid, establishing quantitative measures that characterize the type of flow as laminar or turbulent, this ratio is expressed through the so-called Reynolds number represented by Eq. 3 where u_L and L are the velocity and characteristic dimension of the flow respectively and ν is the kinematic viscosity (Çengel *et al.* 2018).

$$Re = \frac{u_L L}{\nu}. \tag{3}$$

The Reynolds number has a great importance for measuring the relative magnitudes Eq.4 between the inertial term where $\frac{\partial \mathbf{u}}{\partial t}$, and $(\mathbf{u} \cdot \nabla)\mathbf{u}$, represent the temporal variation in velocity and the convective acceleration of the fluid respectively and the viscous term where μ, and $\nabla^2 \mathbf{u}$, represent the kinematic viscosity of the fluid and the momentum respectively (White e Majdalani 2006)

$$\rho \left(\frac{\partial \mathbf{u}}{\partial t} + (\mathbf{u} \cdot \nabla)\mathbf{u} \right) = -\nabla p + \mu \nabla^2 \mathbf{u} + \mathbf{f}, \tag{4}$$

2.1.3 Kinetic Theory

The behavior of a fluid is generally described by physical and mathematical processes that are solved by means of partial differential equations called governing equations for the transport of (mass and momentum) as mentioned above. In order to solve the phenomena involved during the flow of a fluid, part of this physical process must be observed at the molecular level so that a correct understanding of the underlying physics is possible. The theory of kinetic energy takes into account the dynamics that occur between particles obeying Newton's second law for intermolecular forces. Originally the theory was developed for the movement of ideal gases, we know that a molecule has a random movement in a free space and from this movement is extracted the force that will be exerted in a certain direction as it is possible to visualize in Eq. 5 and Eq.6 where F, $\mathbf{c}$, m and t represent respectively the intermolecular forces, unit velocity vector, mass and time illustrated by Fig.1 (Philippi 2024).

$$\mathbf{F} = m \frac{d\mathbf{c}}{dt}, \tag{5}$$

$$\mathbf{c} = \frac{d\mathbf{r}}{dt}, \tag{6}$$

where $\mathbf{r}$ represents the original position of the particle, so when a particle collides with a neighboring particle its velocity $\mathbf{c}$ takes on the value $\mathbf{c} + F dt/m$ and the position of r changes to $r + cdt$ (Brito *et al.* 2017).

Figure 1 – **Intermolecular forces.**

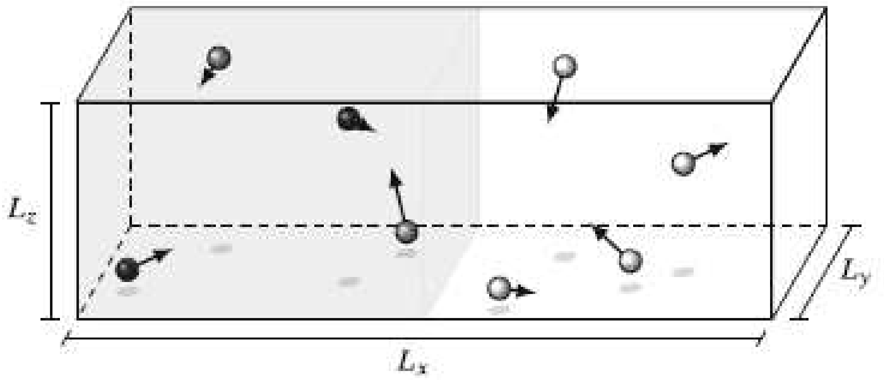

Source: (Kruger 2016).

Mathematical descriptions in fluid dynamics are based on the assumption of continuity operating on length and time scales for the macroscopic scale. When it comes to the particle scale, the following are relevant: the size of an atom or molecule ℓ_a, the mean free path (distance traveled between two successive collisions) ℓ_{mfp}, the analysis of gradients on a macroscopic scale ℓ and the size of the system ℓ_S. The respective time scales are: the collision time (duration of a collision event) t_c, the mean collision time (time between two successive collisions) t_{mfp}, the convection time t_{conv} and the diffusion time t_{diff}. Fig.2 provides an illustrative view of where the mesoscopic level. In mesoscopic kinetic theory, representative collections of particles evolve on time scales around the mean collision time t_{mfp} (Kruger 2016).

Figure 2 – **Representation on macroscopic, mesoscopic and microscopic scales.**

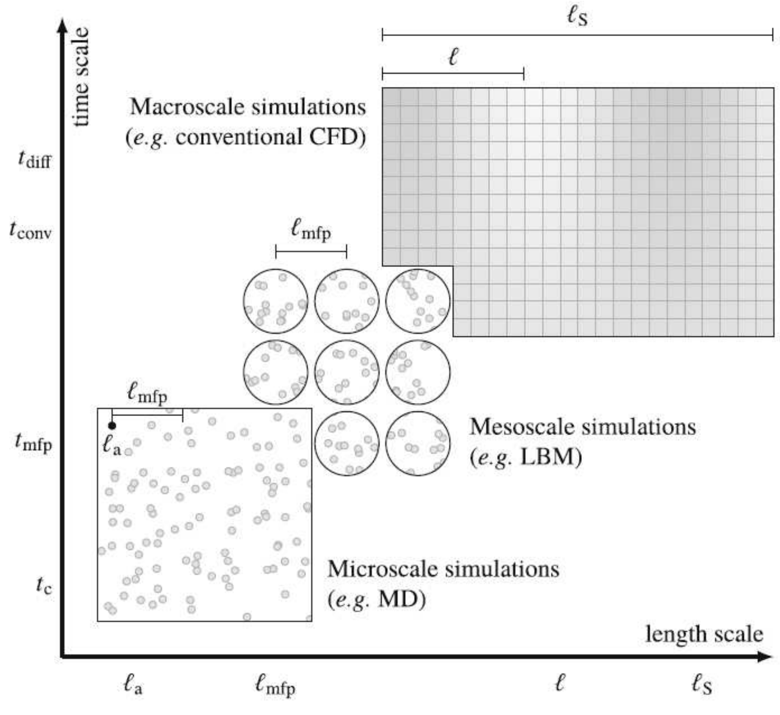

Source: (Kruger 2016).

There are several cases in which the order of the length and time scales is not satisfied, and in order to measure the mean free path so that it becomes large enough to be comparable to the macroscopic length scale, a parameter is used, the Knudsen number Kn.

$$Kn = \frac{\ell_{mfp}}{\ell}, \tag{7}$$

the Kn is a parameter used in Chapman-Enskog theory to derive the Navier-Stokes equations from the Boltzmann equation. The Knudsen number is also related to the Mach and Reynolds numbers.

$$Kn = \alpha \frac{Ma}{Re}. \tag{8}$$

with α being a numerical constant. This relation is known as the von Kármán relation.

2.1.4 The Particle Distribution Function

The essence of kinetic theory is to describe the mesoscopic behavior of a set of particles, using the particle distribution function $f(\mathbf{r}, \xi, t)$. This function provides spatial and temporal information in a microscopic environment for each particle in the system. The particle distribution function is a fundamental variable for kinetic theory, the idea for the system of functions is to correlate information about a set of particles, offering a statistical description of most of the behavior of the particles in a set, and ultimately obtaining macroscopic parameters such as density and velocity from their moments for a given time as can be seen in Eq.9 and Eq.10 (Kruger 2016).

$$\rho(\mathbf{r},t) = \int f(\mathbf{r}, \xi, t)\, \mathrm{d}^3\xi, \tag{9}$$

$$\rho(\mathbf{r},t)\mathbf{u}(\mathbf{r},t) = \int \xi f(\mathbf{r}, \xi, t)\, \mathrm{d}^3\xi, \tag{10}$$

where f, x, ξ, t represent the particle distribution function, position, microscopic velocity and time respectively.

2.1.5 Boltzmann Equation

The Kinetic theory describes the movement of a transiting fluid acting as a bridge between the macroscopic and microscopic scale by tracking the movement of individual particles through the particle distribution function where properties such as position, particle velocity and time are considered. The behavior of the set of particles must obey the governing Navier-Stokes equations in a macroscopic environment. The intermediate scale is also called the mesoscopic scale. The mesoscopic scale is based on the Boltzmann equation, Eq.11, to describe the distribution function of particles through collision, propagation and free movement of particles (Kruger 2016).

$$\frac{df}{dt} = \left(\frac{\partial f}{\partial t}\right) + \left(\frac{\partial f}{\partial x_\beta}\right)\frac{dx_\beta}{dt} + \left(\frac{\partial f}{\partial \xi_\beta}\right)\frac{d\xi_\beta}{dt}, \tag{11}$$

where f is the distribution function in phase space that varies as a function of time t, space x_β, microscopic velocities per ξ_β, the partial derivatives result in a total derivative $\frac{df}{dt}$ known as the collision term and can be described using the BGK (Bhatnagar-Gross-Krook) operator:

$$\Omega = -\frac{f - f^{(0)}}{\tau}. \tag{12}$$

2.2 TURBULENT FLOW

Turbulence is a phenomenon that is commonly observed in everyday life, whether in the smoke expelled from a chimney, in the current of a river or waterfall, or even in gusts of wind (Pope 2013). Turbulent flows are characterized by a large variation of velocity fields in space and time, which occurs in a chaotic manner. (Tennekes e Lumley 1972) detailed turbulent flows using various parameters, including:

Irregularity: An intrinsic characteristic of turbulent flows, irregularity or randomness makes statistical methods a suitable approach for analysis.

Diffusivity: Responsible for the rapid mixing of the fluid with the medium (spreading), as well as increasing the rates of transfer of quantity of movement, heat and mass.

High Reynolds number: Turbulent flows will always occur with a high Reynolds number, which is the ratio between inertial and viscous forces.

In turbulent flow, the velocity field $U(x,y,z)$ can be considered “random”, but this refers to the possibility of a particular time occurring at a particular point. In an experiment that will analyze the flow of a turbulent fluid, the same procedure must occur repeatedly, an example of this can be a certain event $A \equiv \{0 \geq U \geq 1\}$ where U represents a specific component of velocity at a point, if A will inevitably always occur then we take it as a certainty, when A does not occur then it is given as impossible, but when A may or may not occur then it is called random. In turbulent flow we treat velocity as a random variable, so it is necessary to repeat the experiments in order to obtain an average for the cases analyzed and for numerical simulation this result can be obtained by averaging the velocity components over the simulation time (Pope 2013).

2.2.1 Incompressible Flow

Another important macroscopic time scale is acoustic time, $t_{\text{sound}}\ell/c_s$, where c_s is the speed of sound in the fluid. This time scale determines how fast compression waves propagate in the fluid. When the acoustic time is very small compared to the advective time scale, the fluid behaves similarly to an incompressible fluid. Otherwise, the compressibility of the fluid is an important factor, which provides a series of additional phenomena, such as shock waves. The Mach number is given by:

$$Ma = \frac{t_{\text{sound}}}{t_{\text{conv}}}. \qquad (13)$$

For the flow of a fluid in an ideal environment, with low pressures considered and with the speed of the flow considerably lower than the speed of sound propagation in the medium given by the Mach number (Ma), it is possible to consider the variation of zero density for the flow, the relationship between the local speed of the flow and the speed of sound is represented by Eq.14.

$$Ma = \frac{\mathbf{u}}{U_s}, \qquad (14)$$

where U_s is the velocity of sound.

2.2.2 Chapman-Enskog Theory

The Chapman-Enskog analysis expands the particle distribution function in terms of a small parameter ε that represents the relationship between the microscopic scale (associated with kinetic theory and the Boltzmann equation) and the macroscopic scale (associated with hydrodynamic flow and the Navier-Stokes equations).

2.2.3 Turbulent Jet

Several examples of jets are characterized by turbulence, such as water jets, subsonic and supersonic jets, axisymmetric jets, among others (Van Dyke, 1982). In addition, jets are classified as free shear flows, located far from walls, without their influence, and with turbulence arising due to velocity fluctuations (Pope 2013; White e Majdalani 2006).

The flow of a jet is of great importance in understanding natural and technological phenomena. A single-phase jet is characterized by a wide range of movements called fluctuations. Fig.3 shows jets for different Reynolds numbers, and it can be seen that the flow velocity occurs predominantly in the axial direction. It can be seen that after the flow reaches a Re number sufficient to be considered turbulent, this parameter loses relevance as it is raised to larger scales.

In order to obtain a jet, the interaction between a high-pressure environment and a lower-pressure environment is necessary, so the nozzle exit velocity must be the main consideration in order to obtain a correct analysis. In order to obtain an analysis, it is necessary to consider the transition from a confined environment surrounded by walls to an environment that is sufficiently open to be considered a flow at infinity so that the presence of rigid boundaries and recirculations does not affect the flow.

The main characteristics for determining the behavior of a water jet are the exit velocity U_J , the maximum velocity recorded throughout the development of the jet flow U_{max} , the width of the shear layer of the velocity profile $(b_J$, and the viscosity of the fluid ν, so the dimensionless number Re is used to define the flow inlet parameters. As the water jet flow develops, the velocity profile flattens out and the width of the shear layer widens. Taking into account that the jet flow

Figure 3 – **Representation of concentrations in a jet: (a) Re = 5000 and (b) Re = 20000.**

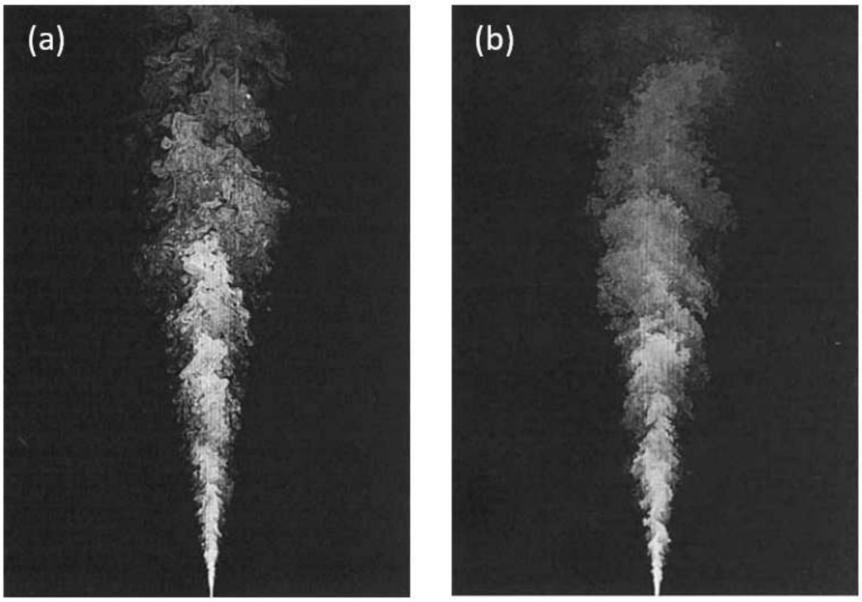

Source: (Dahm e Dimotakis 1990).

occurs in a free environment, the pressure remains constant. The momentum transport generated by a flat jet J is determined using Eq.15.

$$J = \int_{-\infty}^{+\infty} \rho \mathbf{u}^2 dA, \tag{15}$$

where dA refers to an area differential element (White e Majdalani 2006).

The flow of a jet is characterized by three main regions: 1) the inlet region, where the fluid emerges from being injected into a medium; 2) the region of increased mixing and decay of the difference in velocity between the injected fluid and that of the medium into which it was inserted as the jet progresses; 3) the dissipation region, where the velocity of the flow approaches the velocity of the medium, marking the regime in which total mixing occurs between the fluids involved, as shown in Fig.4 (White e Majdalani 2006).

Figure 4 – **Region formation for an axisymmetric turbulent jet.**

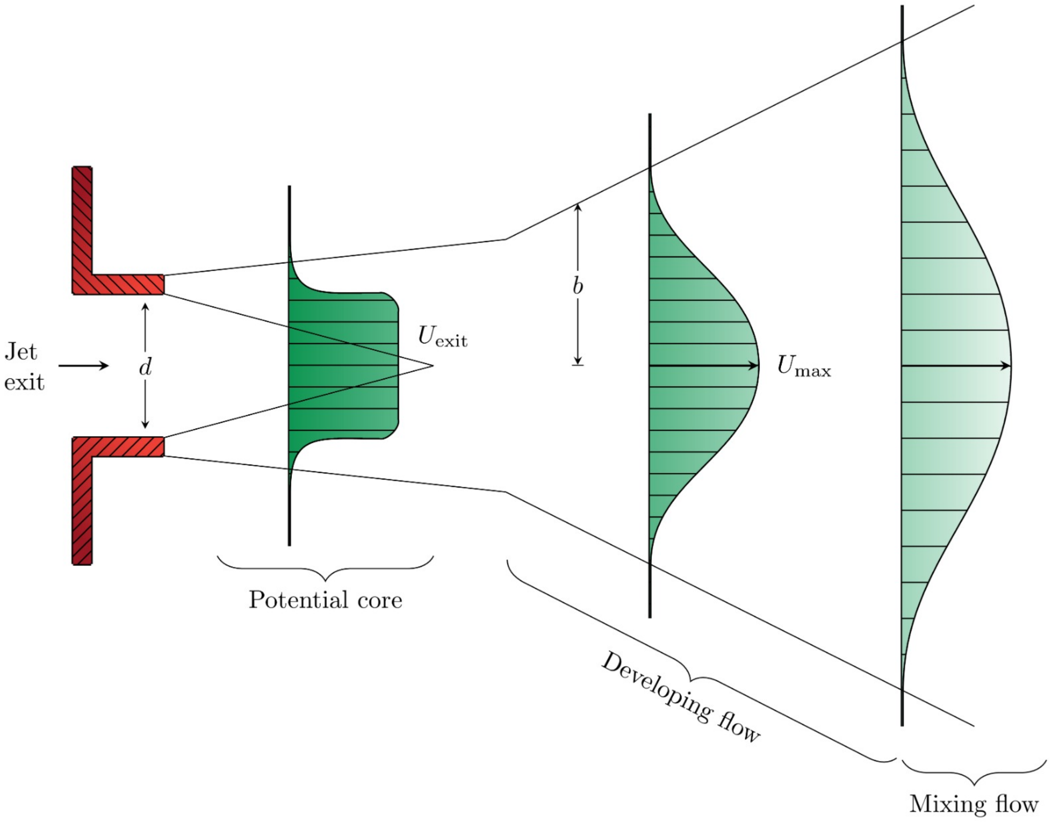

Source: (White e Majdalani 2006).

The concept of self-similarity for an axisymmetric jet is of great importance to verify the validation of the flow in an infinite environment. Self-similarity is obtained through the statistical characteristics in the turbulence region of the jet, this implies the similarity of the decay of the normalized velocity profiles as the distance from the centerline for the entire region of turbulence development (Pope 2013).

2.3 PREVIOUS WORKS

A turbulent jet can be characterized by the continuous flow of a fluid through a nozzle with a diameter D towards an unconfined environment. The main parameters for determining the behavior of a water jet are the exit velocity U_{exit}, the maximum velocity recorded along the development of the jet flow U_{max}, the width of the shear layer of the velocity profile b_{jet} and the Reynolds number Re. The shape of a turbulent jet can be divided into stages where the formation region just after the nozzle is where the fluid is still settling, then there is the development region characterized by the start of mixing between the jet fluid and the ambient fluid and finally the dissipation region where the decay of the velocity and mixing of the fluids will occur (Pope 2013).

2.3.1 Experimental Analysis

The first studies to investigate the behavior of turbulence in a single-phase jet using experimental methods were carried out by (Reichardt 1941) and (Corrsin 1943). Their motivation was to provide results for the velocity profiles, but they were unable to demonstrate the self-preservation of the average velocity profiles along the jet flow. The work carried out by (Wygnanski e Fiedler 1969) described the similarity between the average velocity profiles along the jet's path. This work became a reference for other studies on this subject and was later reviewed by (Rodi 1975; List 1982; Pope 2013).

The work carried out by (Hussein *et al.* 1994) has made important contributions to the analysis of the behavior of turbulent jets, especially in the context of measuring the velocity field for axisymmetric jets with a high Reynolds number. The study presents detailed measurements of the velocity moments up to third order. The experiment was developed in a controlled environment so that it simulates the flow in an infinite domain without significant interference from recirculations and external disturbances, providing a solid and reliable basis for validating the equations of motion for turbulent flow and being used as a reference for future work and numerical models. An important contribution of the work carried out was to demonstrate how the boundary conditions affect the results obtained for the experiment when compared to other studies carried out previously which developed their methods in confined environments and which present significant errors due to the recirculation of the flow.

The results obtained by (Hussein *et al.* 1994) were later used as a reference by the book by (Pope 2013) due to the good agreement between the theoretical predictions and the experimental analysis for the conservation of the amount of movement, kinetic energy and the dissipation of the average of the velocity profiles in the region of the development of jet turbulence normalized by the flow inlet velocity as shown in the graphs in Fig.5 and Fig.6.

Figure 5 – **Radial profiles of the mean axial velocity in a turbulent round jet,** $Re = 1700$**. The dashed lines indicate the half-width** $(r_{1/2(x)})$ **of the profiles where** $\langle U \rangle$ **and** U_J **refer to the average velocity for a plane and the nozzle exit velocity respectively. adapted from data in (Hussein *et al.* 1994).**

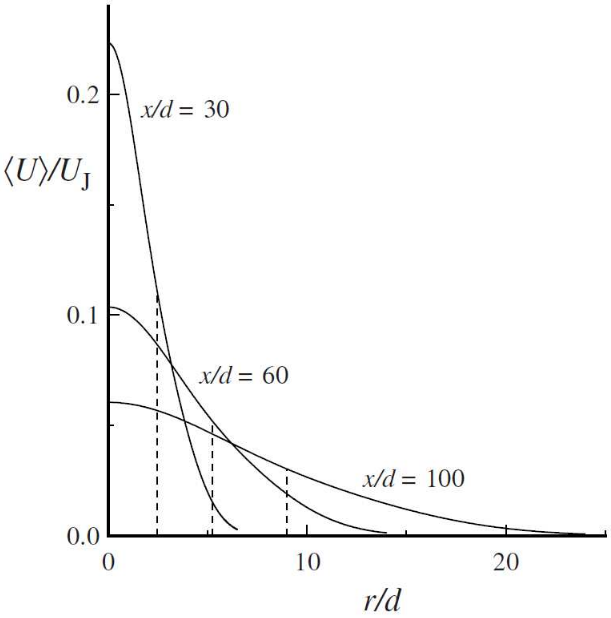

Source: (Hussein *et al.* 1994).

Figure 6 – **Mean axial velocity versus radial distance in a turbulent jet for** $Re = 1700$ **where** U_0 **refers to the centerline velocity. adapted from data in (Wygnanski e Fiedler 1969).**

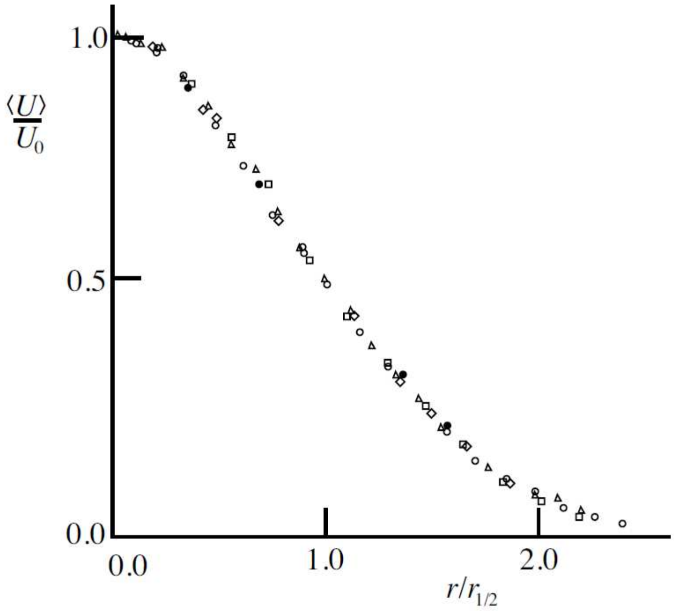

Source: (Wygnanski e Fiedler 1969).

Fig.7 shows the inverse of the velocity decay U_0 in relation to the nozzle exit velocity, U_J for the jet path distance x normalized by the nozzle diameter D, and it is also possible to visualize the results obtained through the experimental method by the points in comparison with the theoretical analytical representation of the result on a straight line. Eq.16 describes the decay of the velocity on the center line of the jet path analytically, where B is an empirical constant for adjusting the line to a value close to 5.8 as described by (Hussein *et al.* 1994).

$$\frac{U_0(x)}{U_J} = \frac{B}{(x-x_0)/D}. \tag{16}$$

Figure 7 – **Variation of mean velocity with axial distance along the centerline in a turbulent jet $Re = 1700$. adapted from data in (Hussein *et al.* 1994).**

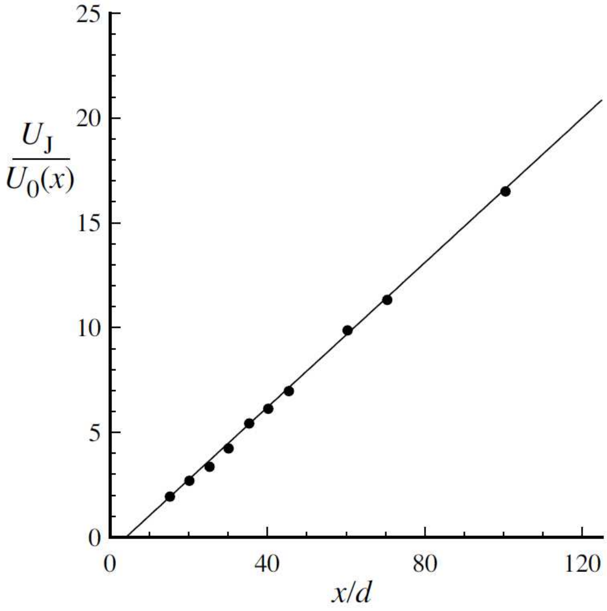

Source: (Hussein *et al.* 1994).

2.3.2 Numerical Analysis

The first numerical simulations developed for turbulent jet flow were carried out between 1960 and 1970 and, due to the computational availability of the time, were limited to the continuum domain with simplified equations and Navier-Stokes derivatives for incompressible fluids. One of the first studies carried out for axisymmetric jets was carried out by (Batchelor e Gill 1962), who provided a mathematical analysis for the stability of a turbulent jet flow without the presence of rigid boundaries. For this case, a sufficiently high Re was considered in order to observe and understand the moment when a jet becomes unstable and how external disturbances influence the turbulence development region.

The study by (Grant 1974) presented one of the first two-dimensional numerical models developed to simulate jet instability, integrating the Navier-Stokes equations over time using the finite difference method. The analysis carried out with this numerical model made it possible to observe how the amplification of disturbances applied to the jet's inlet velocities over time contributes to accelerating the transition of the flow to a turbulent state. The model was validated with experimental methods based on the work carried out by (Beavers e Wilson 1970;

Grant *et al.* 1973), who compared the dimensionless Strouhal number (St), which describes the oscillation in flows that present disturbances and/or vibrations in the formation of the turbulent structure of the jet.

With the advancement of related research and improvements in computer processing power, more accurate and efficient methods have been developed, culminating in techniques that aim to solve turbulent flow on all turbulence scales without simplifications, the work developed by (Panchapakesan e Lumley 1993) provided a detailed analysis that correlates measurements obtained experimentally with the aim of evaluating numerical models for axisymmetric jet flow, especially those developed with a precision of up to 3^{rd} order.

The work developed by (Montessori *et al.* 2024) presents a simulation model based on the high-order Lattice Boltzmann Method (LBM), with a focus on stability in high Reynolds number regimes, which increases the accuracy for the physical representation of turbulent jets. Among the main contributions is the development of an algorithm optimized for execution on GPU architectures, capable of achieving high computational efficiency, with a rate of up to $5x10^{12}$ floating points operations per second (FLOP/s). The proposed model improves the accuracy of the simulations by implementing Hermite polynomials up to the third order $\mathscr{H}^{(3)}_{\alpha\beta\gamma,i}$, which improves the representation of the turbulence region and allows for a better description of the velocity fluctuations. In addition, the study applies the model to an axisymmetric jet with a Reynolds number of 7000, demonstrating that the results obtained are in excellent agreement with experimental data. Another relevant point of the work is the development of new boundary conditions based on non-equilibrium functions and the reconstruction of plots, which enables a more faithful representation of the physical conditions in the computational domain. The implementation of the model also ensures a significant reduction in memory usage, guaranteeing computational efficiency without compromising accuracy, as shown in Fig.8.

Figure 8 – **Panel (a) shows the instantaneous velocity field of the turbulent jet at $Re = 7000$. Panels (b) and (c) show the inverse of the velocity at the centerline (as measured by the inlet velocity). Both graphs show the straight-line behavior that occurs in the development region. Panel (d) shows the average axial velocity profiles at various locations downstream of the nozzle. The profiles fall on the same curve, denoting the self-similarity of the mean axial velocity in turbulent incompressible jets.**

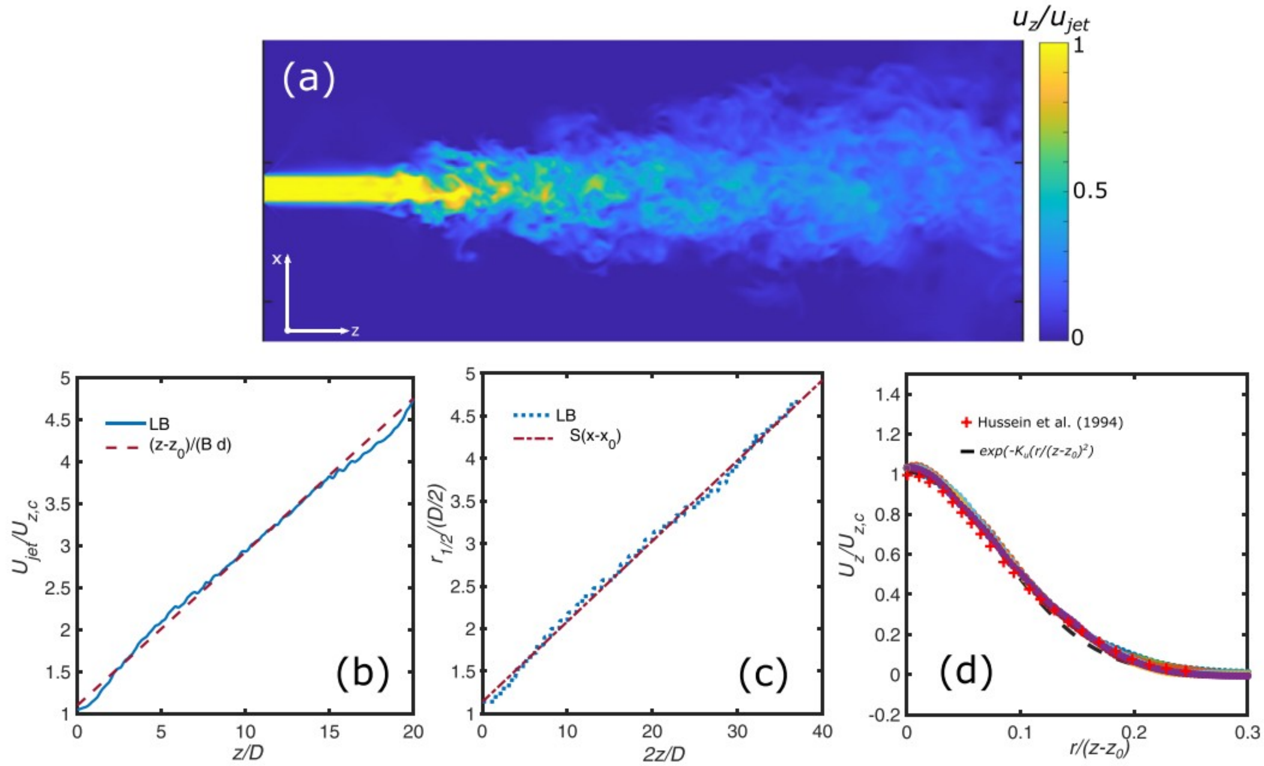

Source: (Montessori *et al.* 2024).

3 METHODOLOGY

3.1 LATTICE BOLTZMANN METHOD

The lattice Boltzmann method involves solving the Boltzmann equation for the hydrodynamic behavior of fluids discretely in velocity and space-time using numerical methods. The LBM method is considered a mesoscopic model for simulating the behavior of fluids, with the ordering and interactions of particles by means of a discrete network. Due to its ability to simulate turbulent flows with complex boundary conditions, the LBM is widely used as an alternative for modeling and computer simulation of fluid dynamics.

Based on kinetic theory, the LBM has its discretization for the so-called phase space, which has coordinates in space $(\mathbf{r})$, time (t) and value of the direction $(\mathbf{c})$. The variable of interest is a particle distribution function $f = f(\mathbf{r}, \mathbf{c}, t)$, which represents the density of particles at each point in the phase space. The LBM operates in two main steps: collision, where a non-linear and local operator is applied; and streaming, which is non-local and linear. The evolution of the particle distribution function $f_i(\mathbf{r},\ t)$, for each microscopic velocity component i.

The distribution function f_i is used to represent the macroscopic properties of a fluid, such as density, as well as the velocity vector of the unit particle c_i at each time step at its respective location. The method consists of initially defining a distribution function for the model domain and successively colliding and propagating the particles, rearranging the mesh at each time step. This process is called the evolution of the distribution function, as can be seen in Eq.17 (Kruger 2016).

$$f_i(r + c_i\Delta t, t + \Delta t) = f_i^{(eq)}(\mathbf{r}, t) + \left(1 - \tau^{-1}\right) \Delta t \hat{f}_i^{(neq)}(\mathbf{r}, t), \tag{17}$$

Considering dimensionless units, the relaxation time τ controls the relaxation time of the viscous stress in the fluid and is linked to the kinematic viscosity ν present in Eq.20. It is possible to replace the last term of the collision equation with Ω:

$$\Delta t \Omega_i(r,t) = \left(1 - \tau^{-1}\right) \Delta t \hat{f}_i^{(neq)}(\mathbf{r}, t), \tag{18}$$

then we define :

$$f_i(r + c_i\Delta t, t + \Delta t) = f_i(r,t) + \Delta t \Omega_i(r,t). \tag{19}$$

$$\omega = \frac{1}{\tau} = \left(a_s^2 \nu + \frac{1}{2}\right)^{-1}, \tag{20}$$

where $a_s = \sqrt{3}$ is a scaling factor based on incompressibility and the speed of sound c_s. Another essential parameter is the pressure, which is calculated using Eq.21.

$$P = c_s^2 \rho. \tag{21}$$

The regularized distribution function is adjusted at each time step and takes into account the density ρ for the moment of order 0, $\rho\mathbf{u}$ for the momentum of order 1^{st}, $\rho m^{(2)}_{\alpha\beta}$ for the moments of order 2^{nd} related to the stress tensor, to update the entire domain (Succi 2001; Hegele.Jr *et al.* 2018).

$$\{\rho, \rho u_\alpha, \rho m^{(2)}_{\alpha\beta}\} = \sum_i g_i \{1, c_{i\alpha}, c_{i\alpha} c_{i\beta} - \delta_{\alpha\beta}/a_s^2\}, \tag{22}$$

where $\delta_{\alpha\beta}$ is the Kronecker delta and $g_i = f_i$ or $\hat{f}_i$; $\hat{f}$ represents the regularized distribution.

The regularization scheme was based on the expansion of Hermite polynomials of up to 2^{nd} order, described by $\mathscr{H}^{(n)}_{\alpha_1 \ldots \alpha_n}$, this set of polynomials is used to discretize the f_i function, bringing it closer to the Maxwell-Boltzmann distribution and allowing it to be represented in terms of macroscopic variables, helping to connect the microscopic dynamics of the particles with the macroscopic properties of the flow.

$$\mathscr{H}^{(0)}_i = 1, \tag{23}$$

$$\mathscr{H}^{(1)}_{\alpha,i} = c_{i\alpha}, \tag{24}$$

$$\mathscr{H}^{(2)}_{\alpha\beta,i} = c_{i\alpha} c_{i\beta} - \frac{\delta_{\alpha\beta}}{a_s^2}. \tag{25}$$

Applying the fourth-order velocity expansion and Hermite polynomials as shown in Fig.9 to the equilibrium function and the regularized non-equilibrium equation during the post-collision step, we obtain Eq.26 and Eq.27, this ensures better numerical stability and accuracy for the simulation.

Figure 9 – **Hermitian representation of refined regularization.**

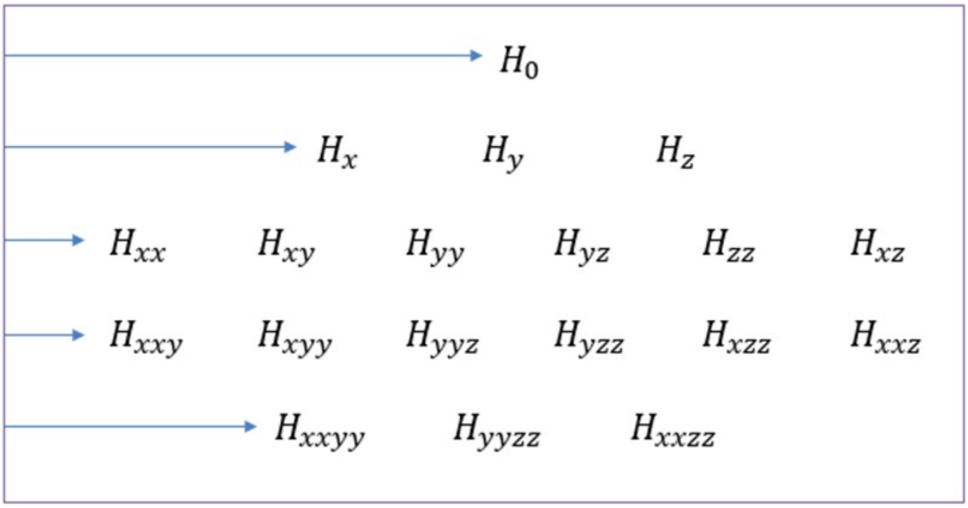

Source: Elaborated by the author (2025).

$$f_i^{(eq)}(r,t) = \rho w_i (1 + a_s^2 u_\alpha c_{i\alpha} + \frac{1}{2} a_s^4 u_\alpha u_\beta \mathscr{H}^{(2)}_{\alpha\beta,i}); \tag{26}$$

$$\hat{f}_i^{(neq)}(r,t) = \frac{1}{2}\rho w_i a_s^4 \left(m_{\alpha\beta}^{(2)} - u_\alpha u_\beta\right) \mathscr{H}_{\alpha\beta,i}^{(2)}. \tag{27}$$

where the viscous stress tensor τ is obtained by calculating the central moments of 2^{nd} order for $f_{(1)}$ and w_i are the quadrature weights which depend on the absolute value of the direction c_i.

$$\Pi_{\alpha\beta} = \int f_{(1)}(c_\alpha - u_\alpha)(c_\beta - u_\beta)\, d\mathbf{c} = \int f_{(1)} c_\alpha c_\beta \, d\mathbf{c} \tag{28}$$

3.1.1 Stencil Models

For the boundary conditions used in the method it is necessary to define a network model used to define the sets of velocities divided into unit components c_i, then information regarding the boundary regions such as faces, edges and corners must be described. Defining the boundary conditions represents the main challenge for simulating cases using the LBM.

Figure 10 – **Representation of the D3Q27 model with the velocity vectors of the stencil pointing from the origin.**

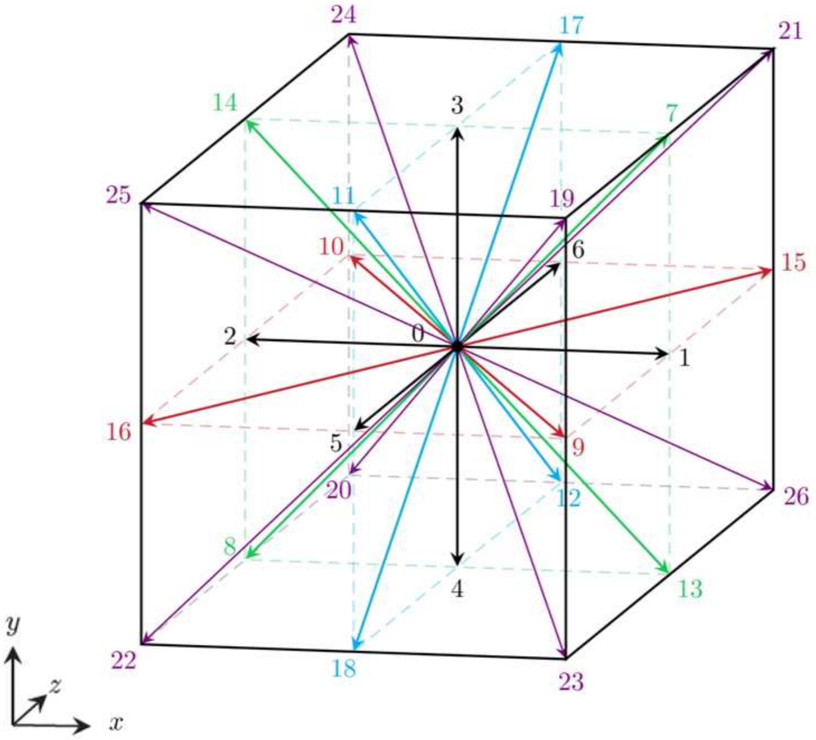

Source: Elaborated by the author (2025).

Figure 11 – **Representation of the D3Q19 model with the velocity vectors of the stencil pointing from the origin.**

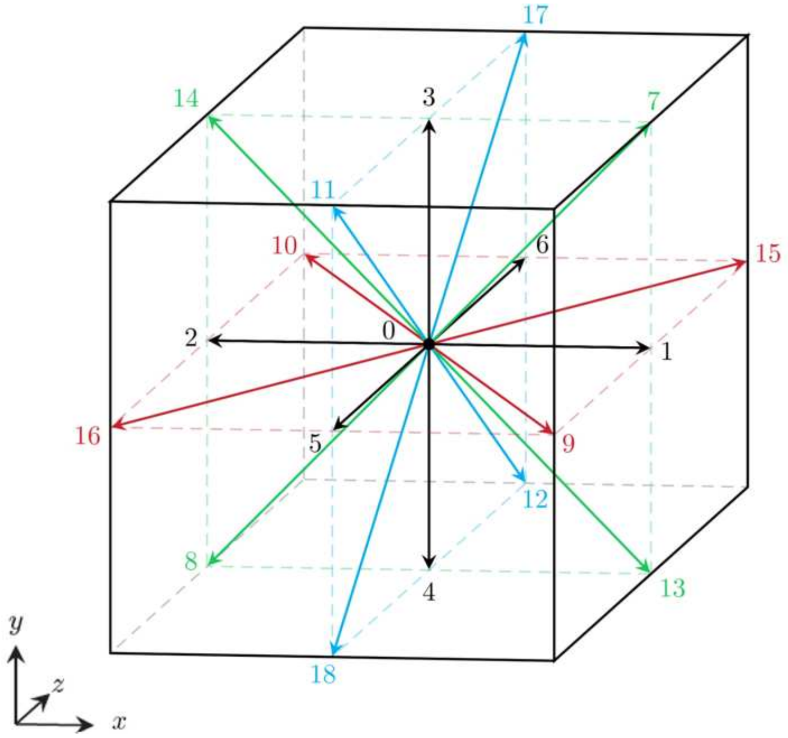

Source: Elaborated by the author (2025).

The model uses a D3Q19 and D3Q27 network as represented by Fig.11 and Fig.10 in which the focal point interacts with the other eighteen neighboring points in the system. Each point in the network is represented by a distribution function f_i which includes the speed and direction of each particle on a microscopic scale, and the sum of this function represents the macroscopic properties of this flow (Kruger 2016).

The discretization of the velocity space transforms the three-dimensional continuum into a reduced set of discrete velocities, while maintaining the characteristics of the macroscopic behavior. Additional parameters are required, where w_i refers to the weight values for each direction indicated and c_i corresponds to the velocity vectors directed towards neighboring locations.

$$w_i = \begin{cases} \frac{1}{3}, & i = 0 \\ \frac{1}{18}, & i = 1,\dots,6 \\ \frac{1}{36}, & i = 7,\dots,18, \end{cases} \tag{29}$$

$$\mathbf{c_i} = \begin{cases} (0,0,0), & i = 0 \\ (\pm1,0,0),\ (0,\pm1,0),\ (0,0,\pm1), & i = 1,\dots,6 \\ (\pm1,\pm1,0),\ (\pm1,0,\pm1),\ (0,\pm1,\pm1), & i = 7,\dots,18, \end{cases} \tag{30}$$

referring to stencil D3Q19

$$
w_i = \begin{cases} \frac{8}{27}, & i = 0 \\ \frac{2}{27}, & i = 1, \ldots, 6 \\ \frac{1}{54}, & i = 7, \ldots, 18 \\ \frac{1}{216}, & i = 19, \ldots, 26, \end{cases} \tag{31}
$$

$$
\mathbf{c_i} = \begin{cases} (0,0,0), & i = 0 \\ (\pm 1,0,0),\ (0,\pm 1,0),\ (0,0,\pm 1), & i = 1, \ldots, 6 \\ (\pm 1,\pm 1,0),\ (\pm 1,0,\pm 1),\ (0,\pm 1,\pm 1), & i = 7, \ldots, 18 \\ (\pm 1,\pm 1,\pm 1), & i = 19, \ldots, 26, \end{cases} \tag{32}
$$

referring to stencil D3Q27.

3.2 BOUNDARY CONDITIONS

3.2.1 Incompressible Regularized Boundary Condition

In the regularization-based boundary condition (RBC), from (Hegele.Jr *et al.* 2018), the regularized distribution function is given by:

$$
\hat{f}_i = \rho w_i \left(1 + a_s^2 u_\alpha c_{i\alpha} + \frac{1}{2} a_s^4 m^{(2)}_{\alpha\beta} \mathscr{H}^{(2)}_{\alpha\beta,i} \right). \tag{33}
$$

In the moment-based lattice Boltzmann method (MRLBM), from (Vardhan *et al.* 2019), we store in the global memory not the distribution function itself, but the moments:

$$
\begin{cases} \sum_i f_i = \rho, \\ \sum_i f_i c_{i\alpha} = \rho u_\alpha, \\ \sum_i f_i \mathscr{H}^{(2)}_{\alpha\beta,i} = \rho m^{(2)}_{\alpha\beta}. \end{cases} \tag{34}
$$

or, for the regularized distribution:

$$
\begin{cases} \sum_i \hat{f}_i = \rho, \\ \sum_i \hat{f}_i c_{i\alpha} = \rho u_\alpha, \\ \sum_i \hat{f}_i \mathscr{H}^{(2)}_{\alpha\beta,i} = \rho m^{(2)}_{\alpha\beta}. \end{cases} \tag{35}
$$

And, given Dirichlet conditions, we know the value of u_α in the boundaries. Thus, we need to calculate ρ and $m^{(2)}_{\alpha\beta}$. Recalling concepts from the RBC (Hegele.Jr *et al.* 2018) for the boundary conditions, we define:

- Incoming populations: particles incoming to the site, $I_s = \{i \mid \mathbf{r} - \mathbf{c}_i$ is a fluid site$\}$,
- Outgoing populations: particles outgoing from the site, $O_s = \{j \mid \mathbf{c}_j = -\mathbf{c}_i, i \in I_s\}$.

If boundary conditions are imposed, they overwrite the moments determined above. Regularized boundary conditions (RBC) are used, conditions based on moments presented in (Hegele.Jr *et al.* 2018). The method involves summing the known and unknown populations and computing the second-order moment:

$$\sum_{i \in I_s} f_i \mathscr{H}^{(2)}_{\alpha\beta,i} + \sum_{i \notin I_s} \hat{f}_i \mathscr{H}^{(2)}_{\alpha\beta,i} = \rho m^{(2)}_{\alpha\beta}. \tag{36}$$

As an example, in Fig.12 we can see the populations that can enter the site of the lower (south) left (west) rear contour of the domain, which in this case are microscopic velocity components c_i for $i = 0,\ 2,\ 4,\ 6,\ 8,\ 10,\ 12$.

Figure 12 – **Example of input populations for a rear south-west corner contour.**

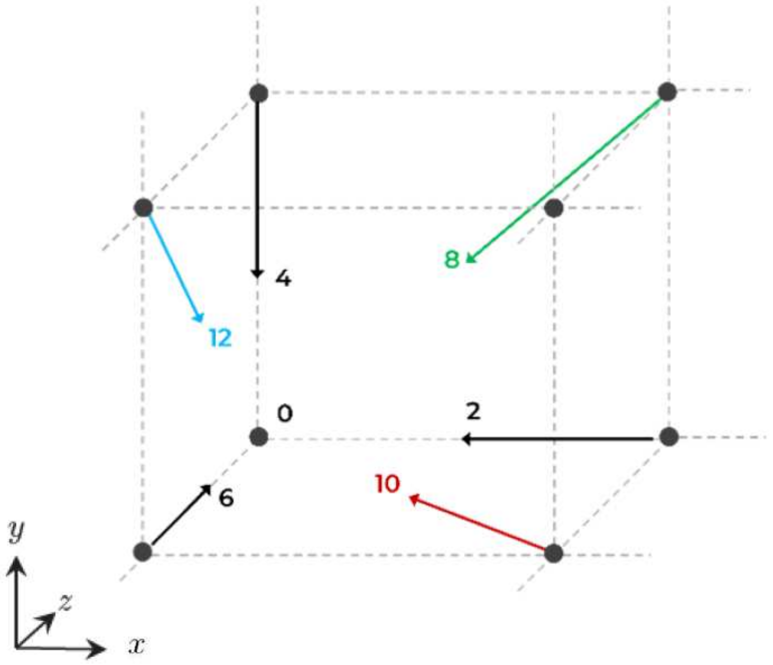

Source: Elaborated by the author (2025).

considering these populations entering the stencil:

$$\rho_I m^{(2)}_{\alpha\beta,I} = \sum_{i \in I_s} \hat{f}_i \mathscr{H}^{(2)}_{\alpha\beta,i}. \tag{37}$$

For Dirichlet boundary conditions (with prescribed variables), this results in six equations for seven variables (moments from 0 to 2^{th} order). To close the system, the last equation is obtained by conserving mass during the collision:

$$\sum_{i\in I_S} f_i = (1-\omega)\sum_{i\in I_{0S}} \hat{f}_i + \omega \sum_{i\in I_S} f_i^{(eq)} \equiv \rho_I, \tag{38}$$

where $\omega = \frac{1}{\tau}$ is the relaxation frequency. The solution of this system of equations allows the values of the moments to be determined, and depends only on the input populations and the network topology.

By adding an incompressibility condition to this model, we can arrive at the incompressible regularized boundary condition (IRBC), a modification that allows us to further improve computational performance ((Bazarin *et al.* 2021; Ferrari e Franco 2024)). To do this, we recall the concept of the strain-rate tensor S, whose components are given by:

$$S_{\alpha\beta} = \frac{1}{2}\left(\frac{\partial u_\alpha}{\partial x_\beta} + \frac{\partial u_\beta}{\partial x_\alpha}\right), \tag{39}$$

within the framework of LBM, it is possible to show that:

$$S_{\alpha\beta} = \frac{a_s^2}{2\tau}\left(u_\alpha u_\beta - m_{\alpha\beta}^{(2)}\right), \tag{40}$$

due to the incompressibility condition, we can see that even on the boundary:

$$\frac{\partial u_x}{\partial x} = 0, \quad \frac{\partial u_y}{\partial y} = 0, \quad \frac{\partial u_z}{\partial z} = 0, \tag{41}$$

and thus $S_{xx} = S_{yy} = S_{zz} = 0$. Thus, in the IRBC, all the normal moments will be equal to the second-order equilibrium moment. In other words, due to the incompressibility condition and Eq.40, $m_{xx}^{(2)} = u_x^2$, $m_{yy}^{(2)} = u_y^2$ e $m_{zz}^{(2)} = u_z^2$.

Also, if $x_{\alpha^\perp}$ and $x_{\beta^\perp}$ are the directions perpendicular to the normal direction x_n of the plane observed in the contour, then it also holds:

$$\frac{\partial u_{\alpha_\perp}}{\partial x_{\beta_\perp}} = 0, \tag{42}$$

and the moments will be $m_{\alpha^\perp\beta^\perp}^{(2)} = u_{\alpha_\perp} u_{\beta_\perp}$. Thus, the second modification of the IRBC is that the moments whose vector of directions of its index is perpendicular to the normal of the plane will also be equal to the second-order equilibrium moment. Any remaining second-order moment will be calculated by Eq.37 and 38.

Once the boundary conditions have been applied, the last step in each iteration is the collision in momentum space, usually carried out using the BGK operator (Bhatnagar *et al.* 1954):

$$\rho' m_{\alpha\beta}^{(2)} = (1-\omega)\rho m_{\alpha\beta}^{(2)} + \omega\rho u_\alpha u_\beta, \tag{43}$$

where the equations of mass and momentum transport correlate if the ratio between ω and the kinematic viscosity ν is:

$$\omega = \frac{1}{\tau} = \left(a_s^2 \nu + \frac{1}{2}\right)^{-1}. \tag{44}$$

3.2.2 Applied Boundary Conditions

One of the main focuses of this work is to define the boundary conditions so that it is possible to simulate the flow of a jet in a domain without interference from rigid boundaries.

To model a 3D axisymmetric jet, a Cartesian domain was adopted with dimensions [L_x, L_y, L_z], corresponding to the coordinates [x, y, z]. The west, east, front and back faces were configured with periodic boundary conditions, while the north face follow Neumann boundary conditions and south faces follow Dirichlet boundary conditions. In the context of the Lattice Boltzmann Method (LBM), the units used to develop the method and analyze the results are dimensionless, defined based on the simulation time steps and the Boltzmann mesh points within the domain.

The Fig.13 shows a schematic representation of the domain, consisting of the following faces: South (S); North (N); East (E); West (W); Front (F); Back (B). It also has a nozzle inlet region located in the center of the S face with a diameter of D and a prescribed velocity of U_{jet}. On the S face, the boundary condition is a dirichlet configuration and on the N face it is a Neumann configuration, while on the W, E, F and B faces the conditions are periodic.

Figure 13 – **Schematic representation of the turbulent jet domain.**

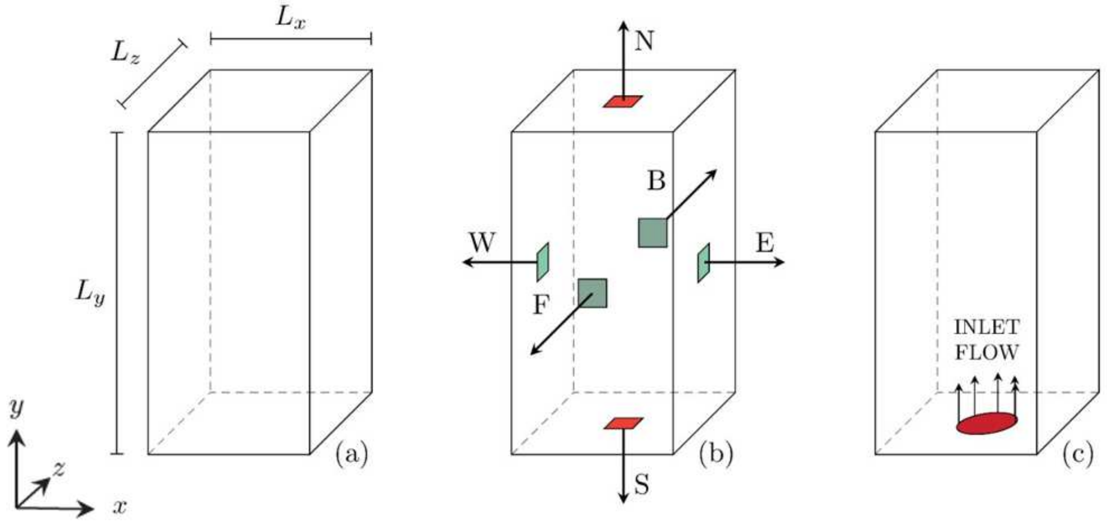

Source: Elaborated by the author (2025).

3.2.2.1 Jet Inlet

For the jet inlet face (Fig.14), the components of the microscopic velocities c_i present in Eq.30 and Eq.32 are highlighted, as shown in Fig. 15, where the values of $i = 0, 1, 2, 4, 5, 6, 8, 9, 10, 12, 13, 15, 16, 18, 20, 22, 23, 26$ for a D3Q27 network model and $i = 0, 1, 2, 4, 5, 6, 8, 9, 10, 12, 13, 15, 16, 18$ for D3Q19, these velocity components can enter through the face with non-positive values for the y axis.

Figure 14 – **Schematic representation of the jet inlet.**

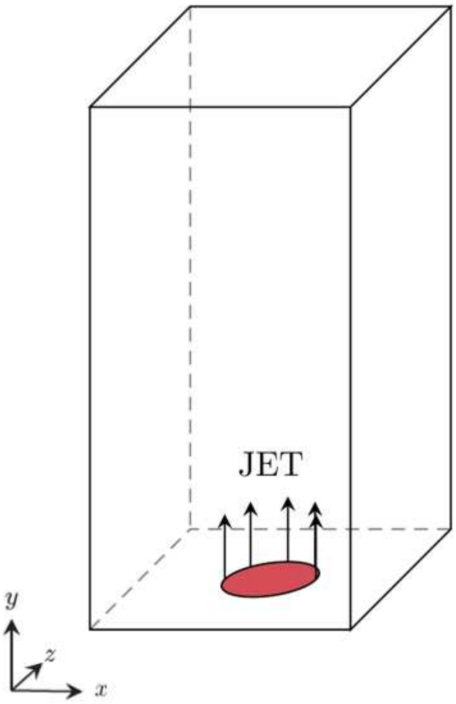

Source: Elaborated by the author (2025).

Figure 15 – **Incoming populations of the jet inlet face, which the set is $O_s =$ 0, 1, 2, 4, 5, 6, 8, 9, 10, 12, 13, 15, 16, 18, 20, 22, 23, 26. for D3Q27 in figure (a), excluding populations $O_s =$ 20, 22, 23, 26. for D3Q19 in figure (b).**

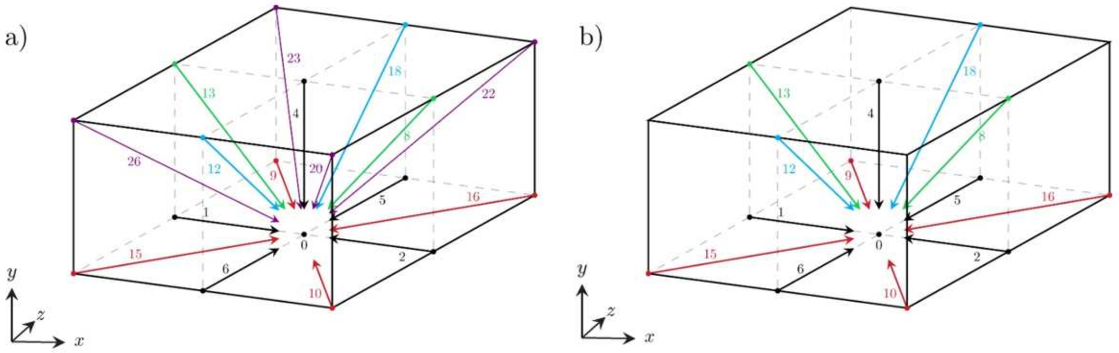

Source: Elaborated by the author (2025).

Figure 16 – **Outgoing populations of the jet inlet face, which the set is $O_s = 0, 1, 2, 3, 5, 6, 7, 9, 10, 11, 14, 15, 16, 17, 19, 21, 24, 25$. for D3Q27 in figure (a), excluding populations $O_s = 19, 21, 24, 25$ for D3Q19 in figure (b)**

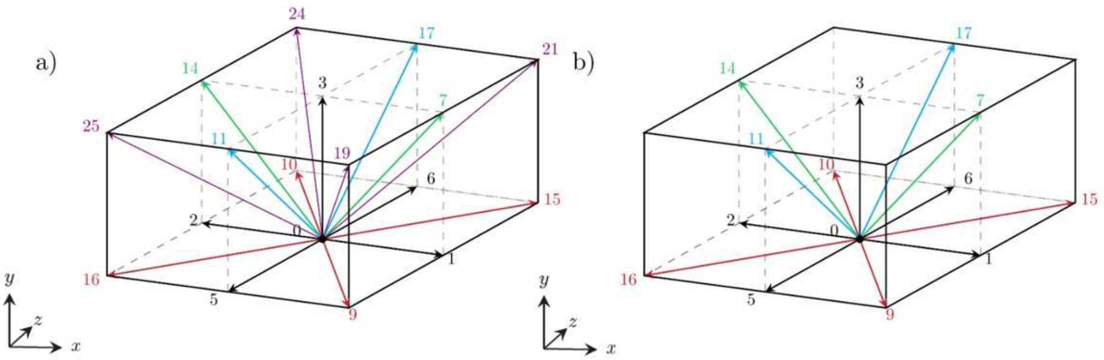

Source: Elaborated by the author (2025).

For the inlet region of the jet, within the framework of the LBM and RBC boundary conditions presented earlier, since there is velocity only in y. The density ρ_I and the second-order moments $m^{(2)}_{\alpha\beta}$ of the remaining inlet are calculated again using Eq.37 and Eq.38. The calculation implemented for the conservation of mass and the second-order moments on this contour follows:

$$\begin{cases} u_x = 0 \\ u_y = U_J \\ u_z = 0 \\ m^{(2)}_{xx} = u_x^2 = 0 \\ m^{(2)}_{yy} = u_y^2 = U_J^2 \\ m^{(2)}_{zz} = u_z^2 = 0 \\ m^{(2)}_{xz} = u_x u_z = 0 \\ m^{(2)}_{xy} = ? \\ m^{(2)}_{yz} = ?, \end{cases} \tag{45}$$

$$\hat{f}_i = w_i \rho \left(1 + \frac{a_s^2}{2} u_\alpha c_{i\alpha} + \frac{a_s^4}{2} m^{(2)}_{\alpha\beta} \mathscr{H}^{(2)}_{\alpha\beta,i}\right), \tag{46}$$

$$f_i^{eq} = w_i \rho \left(1 + a_s^2 \left(u_\alpha c_{i\alpha}\right) + \frac{a_s^4}{2} \left(u_\alpha c_{i\alpha}\right)^2 - \frac{a_s^2}{2} \left(u_\alpha u_\alpha\right)\right), \tag{47}$$

For the conservation of mass at the inlet face of the jet, Eq.38 is used for the variables present in Eq.45 applied in Eq.46 and Eq.47:

$$
\begin{aligned}
\rho_I = (1-\omega) \sum_{i \in O_s} \rho w_i \Bigg(\bigg(1 + \frac{a_s^2}{2} (\cancel{u_x c_{ix}} + u_y c_{iy} + \cancel{u_z c_{iz}} \bigg) \\
+ \frac{a_s^4}{2} \Big(\cancel{m_{xx}^{(2)} \mathscr{H}_{xx,i}^{(2)}} + 2 m_{xy}^{(2)} \mathscr{H}_{xy,i}^{(2)} + \cancel{2 m_{xz}^{(2)} \mathscr{H}_{xz,i}^{(2)}} + m_{yy}^{(2)} \mathscr{H}_{yy,i}^{(2)} + 2 m_{yz}^{(2)} \mathscr{H}_{yz,i}^{(2)} + \cancel{m_{zz}^{(2)} \mathscr{H}_{zz,i}^{(2)}} \Big) \\
+ \omega \Bigg(\sum_{i \in O_s} w_i \rho \left(1 + a_s^2 (\cancel{u_x c_{ix}} + u_y c_{iy} + \cancel{u_z c_{iz}} \right) \\
+ \frac{a_s^4}{2} (\cancel{u_x c_{ix}} + u_y c_{iy} + \cancel{u_z c_{iz}})^2 + \frac{a_s^2}{2} (\cancel{u_x^2} + u_y^2 + \cancel{u_z^2}),
\end{aligned}
\tag{48}
$$

keeping only the variables different from 0 is obtained:

$$
\begin{aligned}
\rho_I = (1-\omega) \sum_{i \in O_s} \rho w_i \left(1 + a_s^2 (u_y c_{iy} \right) + \frac{1}{2} a_s^4 \left(2 m_{xy}^{(2)} \mathscr{H}_{xy,i}^{(2)} + m_{yy}^{(2)} \mathscr{H}_{yy,i}^{(2)} + 2 m_{yz}^{(2)} \mathscr{H}_{yz,i}^{(2)} \right) \\
+ \omega \sum_{i \in O_s} w_i \rho \Bigg(\bigg(1 + a_s^2 (u_y c_{iy}) + \frac{a_s^4}{2} (u_y c_{iy})^2 - \frac{a_s^2}{2} (u_y^2) \bigg) .
\end{aligned}
\tag{49}
$$

Applying the equation obtained to the populations of the D3Q27 and D3Q19 models that exit the inlet face of the jet, we obtain the following result for mass conservation in both cases:

$$
6 \rho_I = \rho (5 + 3 u_y - 3 u_y^2). \tag{50}
$$

For the conservation of second-order moments $m_{\alpha\beta}^{(2)}$ in this case for the axis x, y applied to D3Q27 we have:

$$
\left(\rho m_{\alpha\beta}^{(2)} \right)_I = \hat{f}_0 \left(c_{0\alpha} c_{0\beta} - \frac{\delta_{\alpha\beta}}{a_s^2} \right) + \hat{f}_1 \left(c_{1\alpha} c_{1\beta} - \frac{\delta_{\alpha\beta}}{a_s^2} \right) + \cdots + \hat{f}_{26} \left(c_{26\alpha} c_{26\beta} - \frac{\delta_{\alpha\beta}}{a_s^2} \right), \tag{51}
$$

$$
\begin{aligned}
\rho_I = \sum_{i \in I_s} f_i = f_0 + f_1 + f_2 + f_4 + f_5 + f_6 + f_8 + f_9 + f_{10} + f_{12} + f_{13} + f_{15} + f_{16} \\
+ f_{18} + f_{20} + f_{22} + f_{23} + f_{26},
\end{aligned}
\tag{52}
$$

$$
\begin{aligned}
\left(\rho m_{xy}^{(2)} \right)_I = {} & \hat{f}_0((0)(0)) + \hat{f}_1((1)(0)) + \hat{f}_2((-1)(0)) + \hat{f}_4((0)(-1)) + \hat{f}_5((0)(0)) \\
& + \hat{f}_6((0)(0)) + \hat{f}_8((-1)(-1)) + \hat{f}_9((1)(0)) + \hat{f}_{10}((-1)(0)) \\
& + \hat{f}_{12}((0)(-1)) + \hat{f}_{13}((1)(-1)) + \hat{f}_{15}((1)(0)) \\
& + \hat{f}_{16}((-1)(0)) + \hat{f}_{18}((0)(-1)) + \hat{f}_{20}((-1)(-1)) + \hat{f}_{22}((-1)(-1)) \\
& + \hat{f}_{23}((1)(-1)) + \hat{f}_{26}((1)(-1)),
\end{aligned}
\tag{53}
$$

$$\begin{aligned}\left(\rho m_{yz}^{(2)}\right)_I &= \hat{f}_0((0)(0))+\hat{f}_1((0)(0))+\hat{f}_2((0)(0))+\hat{f}_4((-1)(0))+\hat{f}_5((0)(1))\\ &\quad+\hat{f}_6((0)(-1))+\hat{f}_8((-1)(0))+\hat{f}_9((0)(1))+\hat{f}_{10}((0)(-1))\\ &\quad+\hat{f}_{12}((-1)(-1))+\hat{f}_{13}((-1)(0))+\hat{f}_{15}((0)(-1))\\ &\quad+\hat{f}_{16}((0)(1))+\hat{f}_{18}((-1)(1))+\hat{f}_{20}((-1)(-1))+\hat{f}_{22}((-1)(1))\\ &\quad+\hat{f}_{23}((-1)(1))+\hat{f}_{26}((-1)(-1)),\end{aligned} \tag{54}$$

simplifying for the non-zero terms, we obtain $m_{xy}^{(2)}$ and $m_{yz}^{(2)}$ for D3Q27 at the nozzle inlet the following equation:

$$\left(m_{xy}^{(2)}\right)_I=\frac{\hat{f}_8-\hat{f}_{13}+\hat{f}_{20}+\hat{f}_{22}-\hat{f}_{23}-\hat{f}_{26}}{\rho_I}, \tag{55}$$

$$\left(m_{yz}^{(2)}\right)_I=\frac{\hat{f}_{12}-\hat{f}_{18}+\hat{f}_{20}-\hat{f}_{22}-\hat{f}_{23}+\hat{f}_{26}}{\rho_I}, \tag{56}$$

and for D3Q19 we exclude the velocity components c_i for $i = 19,0,1,2,3,4,5,6$:

$$\left(m_{xy}^{(2)}\right)_I=\frac{\hat{f}_8-\hat{f}_{13}}{\rho_I}, \tag{57}$$

$$\left(m_{yz}^{(2)}\right)_I=\frac{\hat{f}_{12}-\hat{f}_{18}}{\rho_I}. \tag{58}$$

With the input moments defined, it is possible to calculate the global moments based on Eq.37, for $2m_{xz}^{(2)}$ and $2m_{yz}^{(2)}$ in a D3Q27 and D3Q19 network model:

$$\begin{aligned}(\rho m_{xy}^{(2)})_I &= \rho\sum_{i\in I_s} w_i\left(1+a_s^2u_yc_{iy}+\frac{1}{2}a_s^4\left(m_{yy}^{(2)}\mathscr{H}_{yy,i}^{(2)}+2m_{xy}^{(2)}\mathscr{H}_{xy,i}^{(2)}+2m_{yz}^{(2)}\mathscr{H}_{yz,i}^{(2)}\right)\right)\mathscr{H}_{xy,i}^{(2)}\\ &= \rho\sum_{i\in I_s} w_i\left(1+a_s^2u_yc_{iy}+\frac{1}{2}a_s^4\left(m_{yy}^{(2)}\left(c_{iy}c_{iy}-\frac{1}{a_s^2}\right)+2m_{xy}^{(2)}c_{ix}c_{iy}+2m_{yz}^{(2)}c_{iy}c_{iz}\right)\right)c_{ix}c_{iy}.\end{aligned} \tag{59}$$

Using the values obtained in Eq.31 and Eq.32 for $i = 8,\ 13,\ 20,\ 22,\ 23,\ 26$ regarding the weights and microscopic velocities at the nozzle entrance for D3Q27, we obtain:

$$
\begin{aligned}
(\rho m_{xy}^{(2)})_I = \rho w_8 &\left(1 + a_s^2 u_y(-1) + \frac{1}{2}a_s^4\left(m_{yy}^{(2)}(1) - \frac{m_{yy}^{(2)}}{a_s^2} + 2m_{xy}^{(2)}(1) + 2m_{yz}^{(2)}(0)\right)\right)(1) \\
+ \rho w_{13} &\left(1 + a_s^2 u_y(-1) + \frac{1}{2}a_s^4\left(m_{yy}^{(2)}(1) - \frac{m_{yy}^{(2)}}{a_s^2} + 2m_{xy}^{(2)}(-1) + 2m_{yz}^{(2)}(0)\right)\right)(-1) \\
+ \rho w_{20} &\left(1 + a_s^2 u_y(-1) + \frac{1}{2}a_s^4\left(m_{yy}^{(2)}(1) - \frac{m_{yy}^{(2)}}{a_s^2} + 2m_{xy}^{(2)}(1) + 2m_{yz}^{(2)}(1)\right)\right)(1) \\
+ \rho w_{22} &\left(1 + a_s^2 u_y(-1) + \frac{1}{2}a_s^4\left(m_{yy}^{(2)}(1) - \frac{m_{yy}^{(2)}}{a_s^2} + 2m_{xy}^{(2)}(1) + 2m_{yz}^{(2)}(-1)\right)\right)(1) \\
+ \rho w_{23} &\left(1 + a_s^2 u_y(-1) + \frac{1}{2}a_s^4\left(m_{yy}^{(2)}(1) - \frac{m_{yy}^{(2)}}{a_s^2} + 2m_{xy}^{(2)}(-1) + 2m_{yz}^{(2)}(-1)\right)\right)(-1) \\
+ \rho w_{26} &\left(1 + a_s^2 u_y(-1) + \frac{1}{2}a_s^4\left(m_{yy}^{(2)}(1) - \frac{m_{yy}^{(2)}}{a_s^2} + 2m_{xy}^{(2)}(-1) + 2m_{yz}^{(2)}(1)\right)\right)(-1),
\end{aligned}
\tag{60}
$$

$$
\begin{aligned}
(\rho m_{xy}^{(2)})_I = &+ \rho\frac{1}{54}\left(\cancel{+1}\cancel{-a_s^2 u_y}\cancel{+\frac{1}{2}a_s^4 m_{yy}^{(2)}}\cancel{-\frac{1}{2}a_s^4\frac{m_{yy}^{(2)}}{a_s^2}} + \frac{1}{2}a_s^4 2m_{xy}^{(2)}\right) \\
&+ \rho\frac{1}{54}\left(\cancel{-1}\cancel{+a_s^2 u_y}\cancel{-\frac{1}{2}a_s^4 m_{yy}^{(2)}}\cancel{+\frac{1}{2}a_s^4\frac{m_{yy}^{(2)}}{a_s^2}} + \frac{1}{2}a_s^4 2m_{xy}^{(2)}\right) \\
&+ \rho\frac{1}{216}\left(\cancel{+1}\cancel{-a_s^2 u_y}\cancel{+\frac{1}{2}a_s^4 m_{yy}^{(2)}}\cancel{-\frac{1}{2}a_s^4\frac{m_{yy}^{(2)}}{a_s^2}} + \frac{1}{2}a_s^4 2m_{xy}^{(2)}\cancel{+\frac{1}{2}a_s^4 2m_{yz}^{(2)}}\right) \\
&+ \rho\frac{1}{216}\left(\cancel{+1}\cancel{-a_s^2 u_y}\cancel{+\frac{1}{2}a_s^4 m_{yy}^{(2)}}\cancel{-\frac{1}{2}a_s^4\frac{m_{yy}^{(2)}}{a_s^2}} + \frac{1}{2}a_s^4 2m_{xy}^{(2)}\cancel{-\frac{1}{2}a_s^4 2m_{yz}^{(2)}}\right) \\
&+ \rho\frac{1}{216}\left(\cancel{-1}\cancel{+a_s^2 u_y}\cancel{-\frac{1}{2}a_s^4 m_{yy}^{(2)}}\cancel{+\frac{1}{2}a_s^4\frac{m_{yy}^{(2)}}{a_s^2}} + \frac{1}{2}a_s^4 2m_{xy}^{(2)}\cancel{+\frac{1}{2}a_s^4 2m_{yz}^{(2)}}\right) \\
&+ \rho\frac{1}{216}\left(\cancel{-1}\cancel{+a_s^2 u_y}\cancel{-\frac{1}{2}a_s^4 m_{yy}^{(2)}}\cancel{+\frac{1}{2}a_s^4\frac{m_{yy}^{(2)}}{a_s^2}} + \frac{1}{2}a_s^4 2m_{xy}^{(2)}\cancel{-\frac{1}{2}a_s^4 2m_{yz}^{(2)}}\right),
\end{aligned}
\tag{61}
$$

$$
\begin{aligned}
(\rho m_{xy}^{(2)})_I &= \rho\frac{2}{54}\left(+\frac{1}{2}a_s^4 2m_{xy}^{(2)}\right) + \rho\frac{4}{216}\left(+\frac{1}{2}a_s^4 2m_{xy}^{(2)}\right) = \frac{1}{18}\left(+\frac{1}{2}a_s^4 2m_{xy}^{(2)}\right) \\
(\rho m_{xy}^{(2)})_I &= \frac{\rho}{2}m_{xy}^{(2)},
\end{aligned}
$$

using the values obtained in Eq.29 and Eq.30 for $i = 8,\ 13$ regarding the weights and microscopic velocities at the nozzle entrance for D3Q19 we obtain:

$$
\begin{aligned}
(\rho m_{xy}^{(2)})_I = \rho w_{10} &\left(1 + a_s^2 u_y(-1) + \frac{1}{2} a_s^4 \left(m_{yy}^{(2)}(1) - \frac{m_{yy}^{(2)}}{a_s^2} + 2m_{xy}^{(2)}(1) + 2m_{yz}^{(2)}(0) \right) \right)(1) \\
+ \rho w_{15} &\left(1 + a_s^2 u_z(-1) + \frac{1}{2} a_s^4 \left(m_{yy}^{(2)}(1) - \frac{m_{yy}^{(2)}}{a_s^2} + 2m_{xy}^{(2)}(-1) + 2m_{yz}^{(2)}(0) \right) \right)(-1),
\end{aligned}
\tag{62}
$$

$$
\begin{aligned}
&(\rho m_{xy}^{(2)})_I = \rho \frac{1}{36} \left(1 - a_s^2 u_y + \frac{1}{2} a_s^4 m_{yy}^{(2)} - \frac{1}{2} a_s^4 \frac{m_{yy}^{(2)}}{a_s^2} + a_s^4 m_{xy}^{(2)} \right) \\
&+ \rho \frac{1}{36} \left(-1 + a_s^2 u_y - \frac{1}{2} a_s^4 m_{yy}^{(2)} + \frac{1}{2} a_s^4 \frac{m_{yy}^{(2)}}{a_s^2} + a_s^4 m_{xy}^{(2)} \right) \\
&= \rho \frac{1}{36} \left(\cancel{1} - \cancel{a_s^2 u_y} + \cancel{\frac{1}{2} a_s^4 m_{yy}^{(2)}} - \cancel{\frac{1}{2} a_s^4} \frac{\cancel{m_{yy}^{(2)}}}{a_s^2} + a_s^4 m_{xy}^{(2)} - \cancel{1} + \cancel{a_s^2 u_y} - \cancel{\frac{1}{2} a_s^4 m_{yy}^{(2)}} + \cancel{\frac{1}{2} a_s^4} \frac{\cancel{m_{yy}^{(2)}}}{a_s^2} + a_s^4 m_{xy}^{(2)} \right) \\
&= \rho \frac{1}{36} \left(2 a_s^4 m_{xy}^{(2)} \right) \\
&= \rho \frac{1}{36} \left(2 \cdot 9 m_{xy}^{(2)} \right) \\
&= \frac{\rho}{2} m_{xy}^{(2)},
\end{aligned}
\tag{63}
$$

$$
\rho m_{xy}^{(2)} = 2 \rho_I m_{xy,I}^{(2)}, \tag{64}
$$

in a similar way, for $m_{yz}^{(2)}$:

$$
\rho m_{yz}^{(2)} = 2 \rho_I m_{yz,I}^{(2)}, \tag{65}
$$

thus, now we have all the calculations to be implemented for the boundary in the jet inlet:

$$
\rho = \frac{6 \rho_I}{5 + 3u_y - 3u_y^2}, \tag{66}
$$

$$
m_{xy}^{(2)} = \frac{2 \rho_I m_{xy,I}^{(2)}}{\rho}, \tag{67}
$$

$$
m_{yz}^{(2)} = \frac{2 \rho_I m_{yz,I}^{(2)}}{\rho}, \tag{68}
$$

3.2.2.2 South Face

Now let's look at the south face, but at the remaining part of the wall, not at the inlet jet, again highlighting the components of the microscopic velocities for c_i as shown in Fig. 15, where the values of $i = 0,\ 1,\ 2,\ 4,\ 5,\ 6,\ 8,\ 9,\ 10,\ 12,\ 13,\ 15,\ 16,\ 18,\ 20,\ 22,\ 23,\ 26$ for a D3Q27 network model and $i = 0,\ 1,\ 2,\ 4,\ 5,\ 6,\ 8,\ 9,\ 10,\ 12,\ 13,\ 15,\ 16,\ 18$ for D3Q19, these velocity components can enter through the face with non-positive values for the y axis.

Figure 17 – **Schematic representation of the south face.**

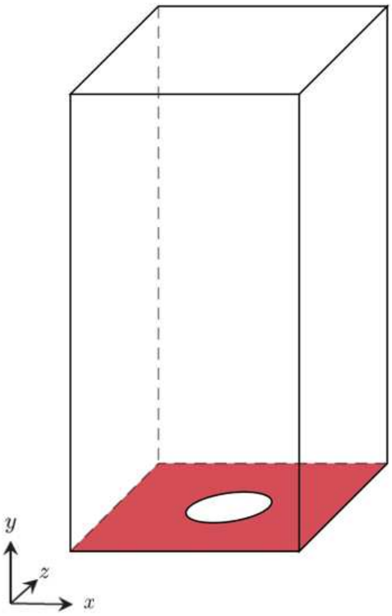

Source: Elaborated by the author (2025).

We know that all the velocities in this case are zero, so for the RBC boundary conditions applied to the southern region, the density ρ_I and second-order moments $m^{(2)}_{\alpha\beta}$ of the remaining input are calculated as follows:

$$\begin{cases} u_x = 0 \\ u_y = 0 \\ u_z = 0 \\ m^{(2)}_{xx} = u_x^2 = 0 \\ m^{(2)}_{yy} = u_y^2 = 0 \\ m^{(2)}_{zz} = u_z^2 = 0 \\ m^{(2)}_{xz} = u_x u_z = 0 \\ m^{(2)}_{xy} = ? \\ m^{(2)}_{yz} = ?, \end{cases} \tag{69}$$

$$\hat{f}_i = w_i \rho \left(1 + \frac{a_s^2}{2} u_\alpha c_{i\alpha} + \frac{a_s^4}{2} m_{\alpha\beta}^{(2)} \mathscr{H}_{\alpha\beta,i}^{(2)} \right), \tag{70}$$

$$f_i^{eq} = w_i \rho \left(1 + a_s^2 \left(u_\alpha c_{i\alpha} \right) + \frac{a_s^4}{2} \left(u_\alpha c_{i\alpha} \right)^2 - \frac{a_s^2}{2} \left(u_\alpha u_\alpha \right) \right), \tag{71}$$

For the conservation of mass on the south face as well as at the jet inlet, Eq.38 is used for the variables present in Eq.69 applied in Eq.70 and Eq.71:

$$\begin{aligned} \rho_I = (1-\omega) \sum_{i \in O_s} \rho w_i & \left(\left(1 + \frac{a_s^2}{2} (\cancel{u_x c_{ix}} + \cancel{u_y c_{iy}} + \cancel{u_z c_{iz}} \right) \right. \\ & + \frac{a_s^4}{2} \left(\cancel{m_{xx}^{(2)} \mathscr{H}_{xx,i}^{(2)}} + 2 m_{xy}^{(2)} \mathscr{H}_{xy,i}^{(2)} + \cancel{2 m_{xz}^{(2)} \mathscr{H}_{xz,i}^{(2)}} + \cancel{m_{yy}^{(2)}} \mathscr{H}_{yy,i}^{(2)} + 2 m_{yz}^{(2)} \mathscr{H}_{yz,i}^{(2)} + \cancel{m_{zz}^{(2)} \mathscr{H}_{zz,i}^{(2)}} \right) \\ & + \omega \left(\sum_{i \in O_s} w_i \rho \left(1 + a_s^2 (\cancel{u_x c_{ix}} + \cancel{u_y c_{iy}} + \cancel{u_z c_{iz}} \right) \right. \\ & + \frac{a_s^4}{2} (\cancel{u_x} c_{ix} + \cancel{u_y c_{iy}} + \cancel{u_z c_{iz}})^2 + \frac{a_s^2}{2} (\cancel{u_x^2} + \cancel{u_y^2} + \cancel{u_z^2}), \end{aligned} \tag{72}$$

preserving only variables other than 0 is obtained:

$$\rho_I = (1-\omega) \sum_{i \in O_s} w_i \rho \left(1 + \frac{1}{2} a_s^4 \left(2 m_{xy}^{(2)} \mathscr{H}_{xy,i}^{(2)} + 2 m_{yz}^{(2)} \mathscr{H}_{yz,i}^{(2)} \right) + \omega \sum_{i \in O_s} w_i \rho . \right. \tag{73}$$

Applying the equation obtained to the populations of models D3Q27 and D3Q19 that exit the south face, we obtain the following result for mass conservation in both cases:

$$\rho_I = 6 \rho (5 + 3 m_{yy}^{(2)} (1 - \omega + 3 u_y - 3 \omega u_y^2)). \tag{74}$$

For the conservation of second-order moments on the south face for ıx▮, ıy▮ applied to D3Q27 and considering populations similar to those present at the entrance to the jet we obtain:

$$\begin{aligned} \rho_I = \sum_{i \in I_s} f_i = {} & f_0 + f_1 + f_2 + f_4 + f_5 + f_6 + f_8 + f_9 + f_{10} + f_{13} + f_{15} + f_{16} + f_{18} \\ & + f_{20} + f_{22} + f_{23} + f_{26}, \end{aligned} \tag{75}$$

we obtain $m_{xy}^{(2)}$ and $m_{yz}^{(2)}$ for D3Q27 on the south face as well as at the entrance of the jet the following equation:

$$\left(m_{xy}^{(2)} \right)_I = \frac{\hat{f}_8 - \hat{f}_{13} + \hat{f}_{20} + \hat{f}_{22} - \hat{f}_{23} - \hat{f}_{26}}{\rho_I}, \tag{76}$$

$$\left(m_{yz}^{(2)} \right)_I = \frac{\hat{f}_{12} - \hat{f}_{18} + \hat{f}_{20} - \hat{f}_{22} - \hat{f}_{23} + \hat{f}_{26}}{\rho_I}, \tag{77}$$

and for D3Q19 we exclude the velocity components c_i for $i = 19, 0, 1, 2, 3, 4, 5, 6$:

$$\left(m_{xy}^{(2)}\right)_I = \frac{\hat{f}_8 - \hat{f}_{13}}{\rho_I}, \tag{78}$$

$$\left(m_{yz}^{(2)}\right)_I = \frac{\hat{f}_{12} - \hat{f}_{18}}{\rho_I}. \tag{79}$$

With the input moments defined, it is possible to calculate the global moments based on Eq.37 for $2m_{xz}^{(2)}$ and $2m_{yz}^{(2)}$ in a D3Q27 and D3Q19 network model:

$$\begin{aligned} (\rho m_{xy}^{(2)})_I &= \rho \sum_{i \in I_s} w_i \left(1 + \frac{1}{2} a_s^4 \left(m_{yy}^{(2)} \mathscr{H}_{yy,i}^{(2)} + 2m_{xy}^{(2)} \mathscr{H}_{xy,i}^{(2)} + 2m_{yz}^{(2)} \mathscr{H}_{yz,i}^{(2)}\right)\right) \mathscr{H}_{xy,i}^{(2)} \\ &= \rho \sum_{i \in I_s} w_i \left(1 + \frac{1}{2} a_s^4 \left(m_{yy}^{(2)} \left(c_{iy} c_{iy} - \frac{1}{a_s^2}\right) + 2m_{xy}^{(2)} c_{ix} c_{iy} + 2m_{yz}^{(2)} c_{iy} c_{iz}\right)\right) c_{ix} c_{iy}. \end{aligned} \tag{80}$$

Using the values obtained in Eq.31 and Eq.32 for $i = 8,\ 13,\ 20,\ 22,\ 23,\ 26$ regarding the weights and microscopic velocities at the nozzle inlet for D3Q27, we obtain:

$$\begin{aligned} (\rho m_{xy}^{(2)})_I = \rho w_8 &\left(1 + \frac{1}{2} a_s^4 \left(2m_{xy}^{(2)}(1) + 2m_{yz}^{(2)}(0)\right)\right)(1) \\ + \rho w_{13} &\left(1 + \frac{1}{2} a_s^4 \left(2m_{xy}^{(2)}(-1) + 2m_{yz}^{(2)}(0)\right)\right)(-1) \\ + \rho w_{20} &\left(1 + \frac{1}{2} a_s^4 \left(2m_{xy}^{(2)}(1) + 2m_{yz}^{(2)}(1)\right)\right)(1) \\ + \rho w_{22} &\left(1 + \frac{1}{2} a_s^4 \left(2m_{xy}^{(2)}(1) + 2m_{yz}^{(2)}(-1)\right)\right)(1) \\ + \rho w_{23} &\left(1 + \frac{1}{2} a_s^4 \left(2m_{xy}^{(2)}(-1) + 2m_{yz}^{(2)}(-1)\right)\right)(-1) \\ + \rho w_{26} &\left(1 + \frac{1}{2} a_s^4 \left(2m_{xy}^{(2)}(-1) + 2m_{yz}^{(2)}(1)\right)\right)(-1), \end{aligned} \tag{81}$$

$$\begin{aligned} (\rho m_{xy}^{(2)})_I = &+ \rho \frac{1}{54} \left(\cancel{+1} + \frac{1}{2} a_s^4 2m_{xy}^{(2)}\right) \\ &+ \rho \frac{1}{54} \left(\cancel{-1} + \frac{1}{2} a_s^4 2m_{xy}^{(2)}\right) \\ &+ \rho \frac{1}{216} \left(\cancel{+1} + \frac{1}{2} a_s^4 2m_{xy}^{(2)} + \cancel{\frac{1}{2} a_s^4 2m_{yz}^{(2)}}\right) \\ &+ \rho \frac{1}{216} \left(\cancel{+1} + \frac{1}{2} a_s^4 2m_{xy}^{(2)} - \cancel{\frac{1}{2} a_s^4 2m_{yz}^{(2)}}\right) \\ &+ \rho \frac{1}{216} \left(\cancel{-1} + \frac{1}{2} a_s^4 2m_{xy}^{(2)} + \cancel{\frac{1}{2} a_s^4 2m_{yz}^{(2)}}\right) \\ &+ \rho \frac{1}{216} \left(\cancel{-1} + \frac{1}{2} a_s^4 2m_{xy}^{(2)} - \cancel{\frac{1}{2} a_s^4 2m_{yz}^{(2)}}\right), \end{aligned} \tag{82}$$

$$
\begin{aligned}
&(\rho m_{xy}^{(2)})_I = \rho\frac{2}{54}\left(+\frac{1}{2}a_s^4 2m_{xy}^{(2)}\right) + \rho\frac{4}{216}\left(+\frac{1}{2}a_s^4 2m_{xy}^{(2)}\right) = \frac{1}{18}\left(+\frac{1}{2}a_s^4 2m_{xy}^{(2)}\right)\\
&(\rho m_{xy}^{(2)})_I = \frac{\rho}{2}m_{xy}^{(2)}.
\end{aligned}
$$

Using the values obtained in Eq.29 and Eq.30 for $i = 8,\ 13$ for the weights and microscopic velocities at the nozzle inlet to D3Q19, we obtain:

$$
\begin{aligned}
(\rho m_{xy}^{(2)})_I = \rho w_8 &\left(1 + \frac{1}{2}a_s^4\left(m_{yy}^{(2)}(1) - \frac{m_{yy}^{(2)}}{a_s^2} + 2m_{xy}^{(2)}(1) + 2m_{yz}^{(2)}(0)\right)\right)(1)\\
+\rho w_{13} &\left(1 + \frac{1}{2}a_s^4\left(m_{yy}^{(2)}(1) - \frac{m_{yy}^{(2)}}{a_s^2} + 2m_{xy}^{(2)}(-1) + 2m_{yz}^{(2)}(0)\right)\right)(-1),
\end{aligned}
\tag{83}
$$

$$
\begin{aligned}
(\rho m_{xy}^{(2)})_I &= \rho\frac{1}{36}\left(1 + \frac{1}{2}a_s^4 m_{yy}^{(2)} - \frac{1}{2}a_s^4\frac{m_{yy}^{(2)}}{a_s^2} + a_s^4 m_{xy}^{(2)}\right)\\
&+\rho\frac{1}{36}\left(-1 - \frac{1}{2}a_s^4 m_{yy}^{(2)} + \frac{1}{2}a_s^4\frac{m_{yy}^{(2)}}{a_s^2} + a_s^4 m_{xy}^{(2)}\right)\\
&= \rho\frac{1}{36}\left(\cancel{1} + \cancel{\frac{1}{2}a_s^4 m_{yy}^{(2)}} - \cancel{\frac{1}{2}a_s^4\frac{m_{yy}^{(2)}}{a_s^2}} + a_s^4 m_{xy}^{(2)} - \cancel{1} - \cancel{\frac{1}{2}a_s^4 m_{yy}^{(2)}} + \cancel{\frac{1}{2}a_s^4\frac{m_{yy}^{(2)}}{a_s^2}} + a_s^4 m_{xy}^{(2)}\right)\\
&= \rho\frac{1}{36}\left(2a_s^4 m_{xy}^{(2)}\right)\\
&= \rho\frac{1}{36}\left(2\cdot 9m_{xy}^{(2)}\right)\\
&= \frac{\rho}{2}m_{xy}^{(2)},
\end{aligned}
\tag{84}
$$

thus, now we have all the calculations to be implemented for the boundary in the south face:

$$\rho = \frac{6\rho_I}{5}, \tag{85}$$

$$m_{xy}^{(2)} = \frac{2\rho_I m_{xy,I}^{(2)}}{\rho}, \tag{86}$$

$$m_{yz}^{(2)} = \frac{2\rho_I m_{yz,I}^{(2)}}{\rho}, \tag{87}$$

3.2.2.3 North Face

Now let's look at the North face, highlighting the components of the microscopic velocities c_i as shown in Fig.19, where the values of $i = 0,\ 1,\ 2,\ 3,\ 5,\ 6,\ 7,\ 9,\ 10,\ 11,\ 14,\ 15,\ 16,\ 17,\ 19,\ 21,\ 24,\ 25$ for a D3Q27 network model and $i = 0,\ 1,\ 2,\ 3,\ 5,\ 6,\ 7,\ 9,\ 10,\ 11,\ 14,\ 15,\ 16,\ 17$ for D3Q19, these velocity components can enter through the face with positive values for the y axis.

Figure 18 – **Schematic representation of the north face.**

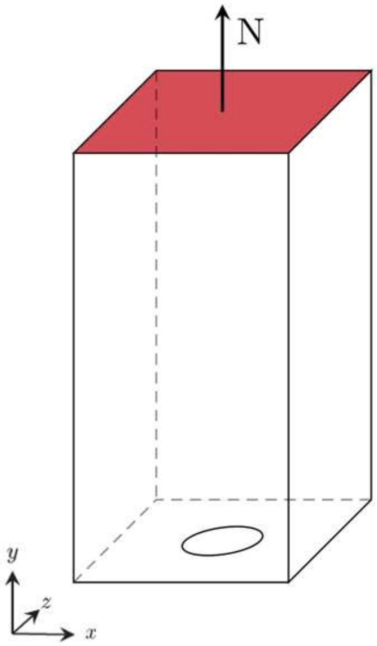

Source: Autoria própria

Figure 19 – **Incoming populations of the north face, which the set is I_s = 0, 1, 2, 3, 5, 6, 7, 9, 10, 11, 14, 15, 16, 17, 19, 21, 24, 25. for D3Q27 in figure (a), excluding populations I_s = 19, 21, 24, 25. for D3Q19 in figure (b).**

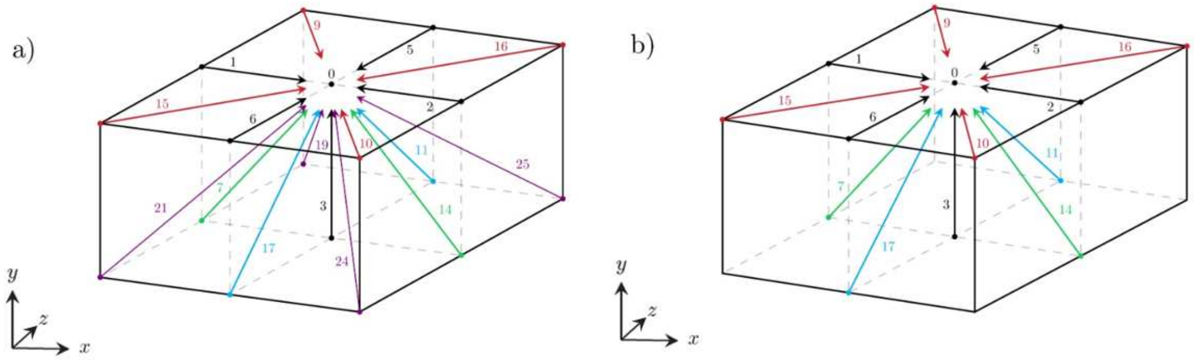

Source: Elaborated by the author (2025).

Figure 20 – **Outgoing populations of the north face, which the set is O_s =0, 1, 2, 4, 5, 6, 8, 9, 10, 12, 13, 15, 16, 18, 20, 22, 23, 26. for D3Q27 in figure (a), excluding populations O_s = 20, 22, 23, 26. for D3Q19 in figure (b).**

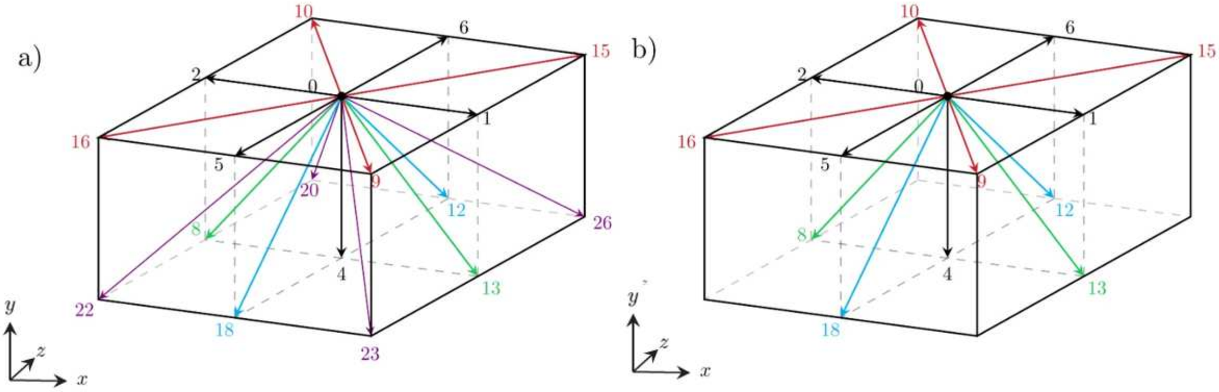

Source: Elaborated by the author (2025).

$$(\rho m^{(2)}_{\alpha\beta})_I = \sum_{i\in I_s} \rho w_i \left(1 + a_s^2 u_\alpha c_{i\alpha} + \frac{1}{2} a_s^4 m^{(2)}_{\alpha\beta} \mathscr{H}^{(2)}_{\alpha\beta,i}\right) \mathscr{H}^{(2)}_{\alpha\beta,i}, \tag{88}$$

where $m^{(2)}_{\alpha\beta}$ in the right-hand side is the global moment. For xy we have:

$$\begin{aligned}(\rho m^{(2)}_{xy})_I = \sum_{i\in I_s} \rho w_i \Bigg(& 1 + a_s^2 (u_x c_{ix} + u_y c_{iy} + u_z c_{iz}) + \frac{1}{2} a_s^4 \\ & \left(m^{(2)}_{xx}\mathscr{H}^{(2)}_{xx,i} + m^{(2)}_{xy}\mathscr{H}^{(2)}_{xy,i} + m^{(2)}_{yy}\mathscr{H}^{(2)}_{yy,i} + m^{(2)}_{yz}\mathscr{H}^{(2)}_{yz,i} + m^{(2)}_{zz}\mathscr{H}^{(2)}_{zz,i}\right)\Bigg) \mathscr{H}^{(2)}_{xy,i}.\end{aligned} \tag{89}$$

For the conservation of second-order moments on the north face for x, y applied to D3Q27 and considering populations similar to those present at the entrance to the jet we obtain:

$$\begin{aligned}\rho_I = \sum_{i\in I_s} f_i = {} & f_0 + f_1 + f_2 + f_3 + f_5 + f_6 + f_7 + f_9 + f_{10} + f_{11} + f_{14} + f_{15} + f_{16} \\ & + f_{17} + f_{19} + f_{21} + f_{24} + f_{25},\end{aligned} \tag{90}$$

$$\begin{aligned}\left(\rho m^{(2)}_{xy}\right)_I = {} & \hat{f}_0((0)(0)) + \hat{f}_1((1)(0)) + \hat{f}_2((-1)(0)) + \hat{f}_3((0)(1)) + \hat{f}_5((0)(0)) \\ & + \hat{f}_6((0)(0)) + \hat{f}_7((1)(1)) + \hat{f}_9((1)(0)) + \hat{f}_{10}((-1)(0)) \\ & + \hat{f}_{11}((0)(1)) + \hat{f}_{14}((-1)(1)) + \hat{f}_{15}((1)(0)) \\ & + \hat{f}_{16}((-1)(0)) + \hat{f}_{17}((0)(1)),\end{aligned} \tag{91}$$

$$\begin{aligned}\left(\rho m^{(2)}_{yz}\right)_I = {} & \hat{f}_0((0)(0)) + \hat{f}_1((0)(0)) + \hat{f}_2((0)(0)) + \hat{f}_3((1)(0)) + \hat{f}_5((0)(1)) \\ & + \hat{f}_6((0)(-1)) + \hat{f}_7((1)(0)) + \hat{f}_9((0)(1)) + \hat{f}_{10}((0)(-1)) \\ & + \hat{f}_{11}((1)(1)) + \hat{f}_{14}((1)(0)) + \hat{f}_{15}((0)(-1)) \\ & + \hat{f}_{16}((0)(-1)) + \hat{f}_{17}((1)(-1)),\end{aligned} \tag{92}$$

we obtain $m_{xy}^{(2)}$ and $m_{yz}^{(2)}$ for D3Q27 on the south face as well as at the entrance of the jet the following equation:

$$\left(m_{xy}^{(2)}\right)_I = \frac{\hat{f}_7 - \hat{f}_{14} + \hat{f}_{19} + \hat{f}_{21} - \hat{f}_{24} - \hat{f}_{25}}{\rho_I}, \tag{93}$$

$$\left(m_{yz}^{(2)}\right)_I = \frac{\hat{f}_{11} - \hat{f}_{17} + \hat{f}_{19} - \hat{f}_{21} - \hat{f}_{24} + \hat{f}_{25}}{\rho_I}, \tag{94}$$

and for D3Q19 we exclude the velocity components c_i for $i = 19,\ 20,\ 21,\ 22,\ 23,\ 24,\ 25,\ 26$: simplifying for the nonzero terms, we obtain for $m_{xy}^{(2)}$ and $m_{yz}^{(2)}$ on the north face the following equation:

$$\left(m_{xy}^{(2)}\right)_I = \frac{\hat{f}_7 - \hat{f}_{14}}{\rho_I}, \tag{95}$$

$$\left(m_{yz}^{(2)}\right)_I = \frac{\hat{f}_{11} - \hat{f}_{17}}{\rho_I}. \tag{96}$$

With the input moments defined, it is possible to calculate the global moments based on Eq.37 for $2m_{xz}^{(2)}$ and $2m_{yz}^{(2)}$ in a D3Q27 and D3Q19 network model:

$$\begin{aligned}(\rho m_{xy}^{(2)})_I &= \rho \sum_{i\in I_s} w_i \left(1 + \frac{1}{2}a_s^4 \left(m_{yy}^{(2)}\mathscr{H}_{yy,i}^{(2)} + 2m_{xy}^{(2)}\mathscr{H}_{xy,i}^{(2)} + 2m_{yz}^{(2)}\mathscr{H}_{yz,i}^{(2)}\right)\right)\mathscr{H}_{xy,i}^{(2)} \\ &= \rho \sum_{i\in I_s} w_i \left(1 + \frac{1}{2}a_s^4 \left(m_{yy}^{(2)}\left(c_{iy}c_{iy} - \frac{1}{a_s^2}\right) + 2m_{xy}^{(2)}c_{ix}c_{iy} + 2m_{yz}^{(2)}c_{iy}c_{iz}\right)\right)c_{ix}c_{iy}.\end{aligned} \tag{97}$$

Using the values obtained in Eq.31 and Eq.32 for $i = 8,\ 13,\ 20,\ 22,\ 23,\ 26$ regarding the weights and microscopic velocities at the nozzle inlet for D3Q27, we obtain:

$$\begin{aligned}(\rho m_{xy}^{(2)})_I = \rho w_7 &\left(1 + \frac{1}{2}a_s^4\left(2m_{xy}^{(2)}(1) + 2m_{yz}^{(2)}(0)\right)(1)\right. \\ +\rho w_{14}&\left(1 + \frac{1}{2}a_s^4\left(2m_{xy}^{(2)}(-1) + 2m_{yz}^{(2)}(0)\right)\right)(-1) \\ +\rho w_{19}&\left(1 + \frac{1}{2}a_s^4\left(2m_{xy}^{(2)}(1) + 2m_{yz}^{(2)}(1)\right)\right)(1) \\ +\rho w_{21}&\left(1 + \frac{1}{2}a_s^4\left(2m_{xy}^{(2)}(1) + 2m_{yz}^{(2)}(-1)\right)\right)(1) \\ +\rho w_{24}&\left(1 + \frac{1}{2}a_s^4\left(2m_{xy}^{(2)}(-1) + 2m_{yz}^{(2)}(-1)\right)\right)(-1) \\ +\rho w_{25}&\left(1 + \frac{1}{2}a_s^4\left(2m_{xy}^{(2)}(-1) + 2m_{yz}^{(2)}(1)\right)\right)(-1),\end{aligned} \tag{98}$$

$$
\begin{aligned}
(\rho m_{xy}^{(2)})_I = &+\rho\frac{1}{54}\left(\cancel{+1}+\frac{1}{2}a_s^4 2m_{xy}^{(2)}\right)\\
&+\rho\frac{1}{54}\left(\cancel{-1}+\frac{1}{2}a_s^4 2m_{xy}^{(2)}\right)\\
&+\rho\frac{1}{216}\left(\cancel{+1}+\frac{1}{2}a_s^4 2m_{xy}^{(2)}+\cancel{\frac{1}{2}a_s^4 2m_{yz}^{(2)}}\right)\\
&+\rho\frac{1}{216}\left(\cancel{+1}+\frac{1}{2}a_s^4 2m_{xy}^{(2)}-\cancel{\frac{1}{2}a_s^4 2m_{yz}^{(2)}}\right)\\
&+\rho\frac{1}{216}\left(\cancel{-1}+\frac{1}{2}a_s^4 2m_{xy}^{(2)}+\cancel{\frac{1}{2}a_s^4 2m_{yz}^{(2)}}\right)\\
&+\rho\frac{1}{216}\left(\cancel{-1}+\frac{1}{2}a_s^4 2m_{xy}^{(2)}-\cancel{\frac{1}{2}a_s^4 2m_{yz}^{(2)}}\right),
\end{aligned}
\tag{99}
$$

$$
\begin{aligned}
&(\rho m_{xy}^{(2)})_I = \rho\frac{2}{54}\left(+\frac{1}{2}a_s^4 2m_{xy}^{(2)}\right)+\rho\frac{4}{216}\left(+\frac{1}{2}a_s^4 2m_{xy}^{(2)}\right)=\frac{1}{18}\left(+\frac{1}{2}a_s^4 2m_{xy}^{(2)}\right)\\
&(\rho m_{xy}^{(2)})_I = \frac{\rho}{2}m_{xy}^{(2)}.
\end{aligned}
$$

Using the values obtained in Eq.29 and Eq.30 for $i = 8,\ 13$ for the weights and microscopic velocities at the nozzle inlet to D3Q19, we obtain:

$$
\begin{aligned}
(\rho m_{xy}^{(2)})_I = \rho w_7\left(1+\frac{1}{2}a_s^4\left(m_{yy}^{(2)}(1)-\frac{m_{yy}^{(2)}}{a_s^2}+2m_{xy}^{(2)}(1)+2m_{yz}^{(2)}(0)\right)\right)(1)\\
+\rho w_{14}\left(1+\frac{1}{2}a_s^4\left(m_{yy}^{(2)}(1)-\frac{m_{yy}^{(2)}}{a_s^2}+2m_{xy}^{(2)}(-1)+2m_{yz}^{(2)}(0)\right)\right)(-1),
\end{aligned}
\tag{100}
$$

$$
\begin{aligned}
(\rho m_{xy}^{(2)})_I &= \rho\frac{1}{36}\left(1+\frac{1}{2}a_s^4 m_{yy}^{(2)}-\frac{1}{2}a_s^4\frac{m_{yy}^{(2)}}{a_s^2}+a_s^4 m_{xy}^{(2)}\right)\\
&+\rho\frac{1}{36}\left(-1-\frac{1}{2}a_s^4 m_{yy}^{(2)}+\frac{1}{2}a_s^4\frac{m_{yy}^{(2)}}{a_s^2}+a_s^4 m_{xy}^{(2)}\right)\\
&=\rho\frac{1}{36}\left(\cancel{1}+\cancel{\frac{1}{2}a_s^4 m_{yy}^{(2)}}-\cancel{\frac{1}{2}a_s^4\frac{m_{yy}^{(2)}}{a_s^2}}+a_s^4 m_{xy}^{(2)}-\cancel{1}-\cancel{\frac{1}{2}a_s^4 m_{yy}^{(2)}}+\cancel{\frac{1}{2}a_s^4\frac{m_{yy}^{(2)}}{a_s^2}}+a_s^4 m_{xy}^{(2)}\right)\\
&=\rho\frac{1}{36}\left(2a_s^4 m_{xy}^{(2)}\right)\\
&=\rho\frac{1}{36}\left(2\cdot 9m_{xy}^{(2)}\right)\\
&=\frac{\rho}{2}m_{xy}^{(2)},
\end{aligned}
\tag{101}
$$

thus, now we have all the calculations to be implemented for the boundary in the north face:

$$\rho = \frac{6\rho_I}{5}, \tag{102}$$

$$m_{xy}^{(2)} = \frac{2\rho_I m_{xy,I}^{(2)}}{\rho}, \tag{103}$$

$$m_{yz}^{(2)} = \frac{2\rho_I m_{yz,I}^{(2)}}{\rho}, \tag{104}$$

3.2.2.4 Periodic Boundary Conditions

The periodic boundary conditions in the LBM connect opposites of a domain, allowing particles leaving one side to automatically enter from the opposite side. This is useful for simulating flows in infinite or cyclic domains. In the context of the domain developed for the turbulent jet, the W, E, F and B faces were considered as periodic boundary conditions.

3.2.2.5 Sponge Layer

For the outlet boundary conditions, it is necessary for the boundaries to minimize the reflection of the flow into the domain. One way to reduce this reflection is by using methods that dissipate the vortices near the boundary, creating a sponge zone which is set up as a damping region to reduce the velocity fluctuations near the outlet, in the sponge zone a higher kinematic viscosity is imposed (Xue *et al.* 2022; Montessori *et al.* 2024).

The region in Fig.21 at the end of the domain on the "y" axis represents the simulation's sponge zone, which is set to $5D$.

Figure 21 – **Representation of the sponge region.**

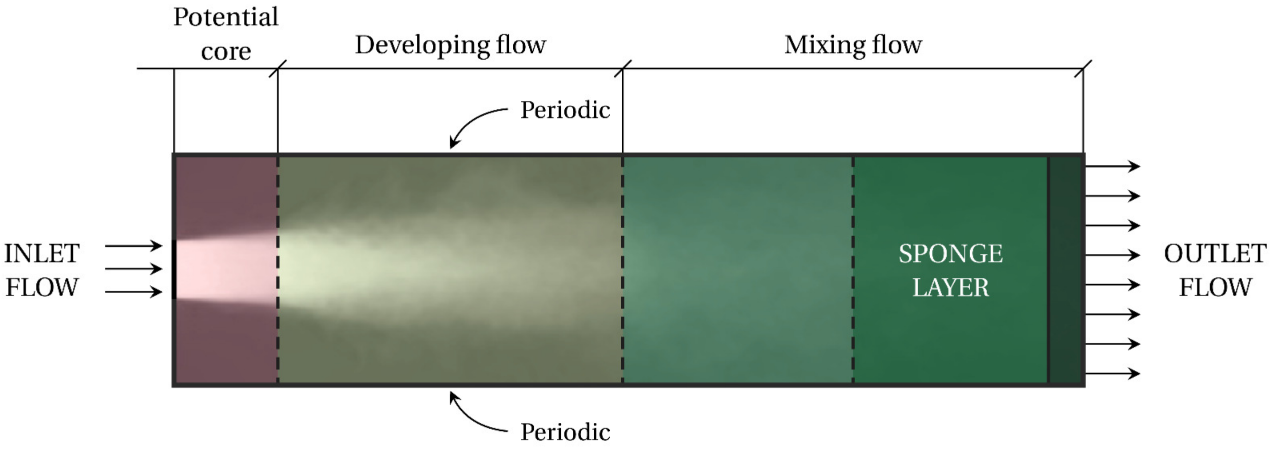

Source: Elaborated by the author (2025).

$$\nu_{\text{sponge}} = \nu_{\text{eff}} \left[K \left(\frac{y - y_{\text{start}}}{y_{\text{end}} - y_{\text{start}}} \right)^p + 1 \right], \tag{105}$$

where K and p are empirical constants, ν_{eff} is the viscosity applied to the other regions of the model, lattice Boltzmann, y_{start} and y_{end} are the start point and end point of the sponge zone, respectively. The empirical constants are set at $K = 1000$ and $p = 3$ to ensure the stability of the simulation (Xue *et al.* 2022).

3.2.3 Chapman-Enskog analysis

3.2.3.1 Taylor series expansion

Using Chapman-Enskog analysis, the expansion in Hermite polynomials is used to derive the Navier-Stokes equations from the LBM model. This derivation shows how the method recovers the macroscopic equations of fluid motion from the kinetic theory equations. We begin the analysis by expanding the equation for the evolution of the particle distribution function into Taylor series where:

$$f_i(r+c_i\Delta t, t+\Delta t) = f_i^{eq}(r,t) + \Delta t \frac{Df_i}{Dt} + \frac{1}{2}\Delta t^2 \frac{D^2 f_i}{Dt^2} + \mathscr{O}(\Delta t^3), \tag{106}$$

isolating the collision term Ω from Eq.19 we get:

$$\begin{aligned} \Delta t \Omega_i &= \Delta t \frac{Df_i}{Dt} + \frac{1}{2}\Delta t^2 \frac{D^2 f_i}{Dt^2} + \mathscr{O}(\Delta t^3), \\ \Omega_i &= \frac{Df_i}{Dt} + \frac{1}{2}\Delta t \frac{D^2 f_i}{Dt^2} + \mathscr{O}(\Delta t^2), \end{aligned} \tag{107}$$

we may multiply the above equation by $\frac{1}{2}\Delta t \frac{D}{Dt}$ to get:

$$\begin{aligned} \frac{1}{2}\Delta t \frac{D}{Dt}\Omega_i(r,t) &= \frac{1}{2}\Delta t \frac{D^2}{Dt^2} f_i + \frac{1}{4}\Delta t^2 \frac{D^3}{Dt^3} f_i + \mathscr{O}(\Delta t^3) = \\ &= \frac{1}{2}\Delta t \frac{D^2}{Dt^2} f_i + \mathscr{O}(\Delta t^2), \end{aligned} \tag{108}$$

where the last equality holds because we have dropped terms with order Δt^2 and higher.

Then, we substitute this result to get:

$$\frac{D}{Dt} \equiv \frac{\partial}{\partial t} + c_{i\alpha}\frac{\partial}{\partial x_\alpha}, \tag{109}$$

$$\Omega_i = \left(\frac{\partial}{\partial t} + c_{i\alpha}\frac{\partial}{\partial x_\alpha}\right) f_i + \frac{1}{2}\Delta t \left(\frac{\partial}{\partial t} + c_{i\alpha}\frac{\partial}{\partial x_\alpha}\right)^2 f_i + \mathscr{O}(\Delta t^2), \tag{110}$$

by $\left(\frac{\partial}{\partial t} + c_{i\alpha}\frac{\partial}{\partial x_\alpha}\right)^2$ we mean:

$$\left(\frac{\partial}{\partial t} + c_{i\alpha}\frac{\partial}{\partial x_\alpha}\right)^2 = \frac{\partial^2}{\partial t^2} + 2c_{i\alpha}\frac{\partial^2}{\partial x_\alpha \partial t} + c_{i\alpha}c_{i\beta}\frac{\partial^2}{\partial x_\alpha \partial x_\beta}, \tag{111}$$

then:

$$\Omega_i(r,t) = \left(\frac{\partial}{\partial t} + c_{i\alpha}\frac{\partial}{\partial x_\alpha}\right) f_i + \frac{1}{2}\Delta t \left(\frac{\partial^2}{\partial t^2} + 2c_{i\alpha}\frac{\partial^2}{\partial x_\alpha \partial t} + c_{i\alpha}c_{i\beta}\frac{\partial^2}{\partial x_\alpha \partial x_\beta}\right) f_i, \tag{112}$$

where we have dropped the $\mathscr{O}(\Delta t^2)$ term for convenience.

3.2.3.2 Scale Analysis

We proceed now with a scale analysis for the equation above. It is important to remember that we are now using lattice variables, the lattice collision time, mean free path and time in the lattice can be written as then:

$$\overline{c} = \frac{\ell}{\tau_c}; \quad t_c = \frac{L}{U}, \tag{113}$$

where $\overline{c}$ is the characteristic velocity of the particle in the lattice, τ_c is the collision time of the lattice, ℓ is the mean free path of the lattice, L, t_c, U are the characteristic length, time and velocity of the lattice, we also define that $\overline{f}$ is the characteristic particle distribution function. We can now propose non-dimensional variables based on the above definitions:

$$\begin{aligned} C_{i\alpha} = \frac{c_{i\alpha}}{\overline{c}}; \qquad t_D = \frac{t}{t_c}; \qquad \chi_\alpha = \frac{x_\alpha}{L}; \\ \Delta t_D = \frac{\Delta t}{\tau_c}; \quad \Omega_{i,D} = \frac{\Omega_i \tau_c}{\overline{f}}, \end{aligned} \tag{114}$$

we can now substitute in Eq.112 so that we get:

$$\begin{aligned} \Omega_{i,D}\frac{\overline{f}}{\tau_c} &= \left(\frac{\partial}{\partial t_D t_c} + \overline{c}C_{i\alpha}\frac{\partial}{\partial \chi_\alpha L}\right) f_i + \frac{\tau_c}{2\Delta t_D}\left(\frac{1}{t_c^2}\frac{\partial^2}{\partial t_D^2} + 2\overline{c}C_{i\alpha}\frac{1}{Lt_c}\frac{\partial^2}{\partial \chi_\alpha \partial t_D} + \overline{c}^2 C_{i\alpha}C_{i\beta}\frac{1}{L^2}\frac{\partial^2}{\partial \chi_\alpha \partial \chi_\beta}\right) f_i \Rightarrow \\ \Omega_{i,D}\overline{f} &= \left(\frac{\tau_c}{t_c}\frac{\partial}{\partial t_D} + \tau_c\overline{c}C_{i\alpha}\frac{1}{L}\frac{\partial}{\partial \chi_\alpha}\right) f_i + \frac{1}{2\Delta t_D}\left(\frac{\tau_c^2}{t_c^2}\frac{\partial^2}{\partial t_D^2} + 2\overline{c}C_{i\alpha}\frac{\tau_c^2}{Lt_c}\frac{\partial^2}{\partial \chi_\alpha \partial t_D} + \overline{c}^2 C_{i\alpha}C_{i\beta}\frac{\tau_c^2}{L^2}\frac{\partial^2}{\partial \chi_\alpha \partial \chi_\beta}\right) f_i = \\ &= \left(\frac{\tau_c}{t_c}\frac{\partial}{\partial t_D} + C_{i\alpha}\frac{l}{L}\frac{\partial}{\partial \chi_\alpha}\right) f_i + \frac{1}{2\Delta t_D}\left(\frac{\tau_c^2}{t_c^2}\frac{\partial^2}{\partial t_D^2} + 2C_{i\alpha}\frac{\tau_c l}{Lt_c}\frac{\partial^2}{\partial \chi_\alpha \partial t_D} + C_{i\alpha}C_{i\beta}\frac{l^2}{L^2}\frac{\partial^2}{\partial \chi_\alpha \partial \chi_\beta}\right) f_i. \end{aligned} \tag{115}$$

Now we should take into account the Knudsen number, ε a relation between the mean free path of the particles and the characteristic length:

$$\begin{aligned} \varepsilon &= \frac{\ell}{L}, \\ \frac{\ell}{L} &\approx \frac{\tau_c}{t_c}, \\ \overline{c} &\approx U, \end{aligned} \tag{116}$$

applying Eq.115 and based on Eq.109 we obtain:

$$\begin{aligned}\Omega_{i,D}\overline{f} &= \varepsilon\left(\frac{\partial}{\partial t_D}+C_{i\alpha}\frac{\partial}{\partial \chi_\alpha}\right)f_i+\frac{1}{2}\Delta t_D\varepsilon^2\left(\frac{\partial^2}{\partial t_D^2}+2C_{i\alpha}\frac{\partial^2}{\partial\chi_\alpha\partial t_D}+C_{i\alpha}C_{i\beta}\frac{\partial^2}{\partial\chi_\alpha\partial\chi_\beta}\right)f_i,\\ \Omega_{i,D}\overline{f} &= \varepsilon\frac{Df_i}{Dt}+\frac{1}{2}\Delta t_D\varepsilon^2\frac{D^2f_i}{Dt^2}.\end{aligned} \tag{117}$$

Now we will define the collision operator. We will use the BGK collision operator as:

$$\begin{aligned}\Omega_{i,D}\overline{f} &= \frac{f_i^{(eq)}-f_i}{\tau}\tau_c\\ &= \frac{f_i^{(eq)}-f_i}{\tau_D},\end{aligned} \tag{118}$$

where $\tau_D = \tau/\tau_c$. Substituting the BGK approximation we have:

$$f_i^{(eq)}-f_i = \varepsilon\frac{D}{Dt}\left(\tau_D f_i+\frac{1}{2}\Delta t_D\left(f_i^{(eq)}-f_i\right)\right). \tag{119}$$

3.2.3.3 Expansion in powers of Knudsen

Now we expand the particle distribution function in powers of ε:

$$f_i = f_i^{(0)}+\varepsilon f_i^{(1)}+\varepsilon^2 f_i^{(2)}+... \tag{120}$$

to get:

$$\begin{aligned}f_i^{(eq)}-\left(f_i^{(0)}+\varepsilon f_i^{(1)}+\varepsilon^2 f_i^{(2)}\right) &= \varepsilon\frac{D}{Dt}\left(\tau_D\left(f_i^{(0)}+\varepsilon f_i^{(1)}+\varepsilon^2 f_i^{(2)}\right)+\frac{1}{2}\Delta t_D\left(f_i^{(eq)}-\left(f_i^{(0)}+\varepsilon f_i^{(1)}+\varepsilon^2 f_i^{(2)}\right)\right)\right)\\ &= \varepsilon\frac{D}{Dt}\left(\tau_D\left(f_i^{(0)}+\varepsilon f_i^{(1)}\right)+\frac{1}{2}\Delta t_D\left(f_i^{(eq)}-\left(f_i^{(0)}+\varepsilon f_i^{(1)}\right)\right)\right)+\mathcal{O}\left(\varepsilon^3\right)\\ f_i^{(eq)}-f_i^{(0)}-\varepsilon f_i^{(1)}-\varepsilon^2 f_i^{(2)} &= \frac{D}{Dt}\left(\tau_D\varepsilon f_i^{(0)}+\tau_D\varepsilon^2 f_i^{(1)}+\frac{1}{2}\Delta t_D\left(\varepsilon f_i^{(eq)}-\varepsilon f_i^{(0)}-\varepsilon^2 f_i^{(1)}\right)\right).\end{aligned} \tag{121}$$

Now we should solve for equal orders of the parameter ε. Then, for the order zero of ε:

$$f_i^{(eq)}-f_i^{(0)} = 0, \tag{122}$$

the $f_i^{(0)}$ is the maxwellian equilibrium distribution function. This result leads to:

$$\begin{aligned}-\varepsilon f_i^{(1)}-\varepsilon^2 f_i^{(2)} &= \frac{D}{Dt}\left(\tau_D\varepsilon f_i^{(0)}+\tau_D\varepsilon^2 f_i^{(1)}+\frac{1}{2}\Delta t_D\left(-\varepsilon^2 f_i^{(1)}\right)\right) =\\ &= \frac{D}{Dt}\left(\tau_D\varepsilon f_i^{(0)}+\varepsilon^2 f_i^{(1)}\left(\tau_D-\frac{1}{2}\Delta t_D\right)\right).\end{aligned} \tag{123}$$

Now, the ansatz for the time derivative:

$$\frac{\partial}{\partial t_D} \equiv \frac{\partial}{\partial t_{D,0}}+\varepsilon\frac{\partial}{\partial t_{D,1}}, \tag{124}$$

so:

$$\frac{D}{Dt}=\frac{\partial}{\partial t_{D,0}}+C_{i\alpha}\frac{\partial}{\partial \chi_\alpha}+\varepsilon\frac{\partial}{\partial t_{D,1}}, \tag{125}$$

and we get:

$$\begin{aligned}-\varepsilon f_i^{(1)}-\varepsilon^2 f_i^{(2)}&=\left(\frac{\partial}{\partial t_{D,0}}+C_{i\alpha}\frac{\partial}{\partial \chi_\alpha}+\varepsilon\frac{\partial}{\partial t_{D,1}}\right)\left(\tau_D\varepsilon f_i^{(0)}+\varepsilon^2 f_i^{(1)}\left(\tau_D-\frac{1}{2}\Delta t_D\right)\right)=\\&=\left(\frac{\partial}{\partial t_{D,0}}+C_{i\alpha}\frac{\partial}{\partial \chi_\alpha}\right)\left(\tau_D\varepsilon f_i^{(0)}+\varepsilon^2 f_i^{(1)}\left(\tau_D-\frac{1}{2}\Delta t_D\right)\right)+\left(\varepsilon\frac{\partial}{\partial t_{D,1}}\right)\left(\tau_D\varepsilon f_i^{(0)}\right).\end{aligned} \tag{126}$$

Now we should divide the first and second order terms in ε. For the first order in ε we have:

$$-f_i^{(1)}=\tau_D\left(\frac{\partial}{\partial t_{D,0}}+C_{i\alpha}\frac{\partial}{\partial \chi_\alpha}\right)f_i^{(0)}. \tag{127}$$

and for the second order in ε we have:

$$-f_i^{(2)}=\left(\frac{\partial}{\partial t_{D,0}}+C_{i\alpha}\frac{\partial}{\partial \chi_\alpha}\right)\left(\tau_D-\frac{1}{2}\Delta t_D\right)f_i^{(1)}+\tau_D\frac{\partial}{\partial t_{D,1}}f_i^{(0)}. \tag{128}$$

Now we have discovered a set of equations which can be used to solve recursively $f^{(n)}$. If we know $f^{(0)}$, we can use Eq.127 to solve $f^{(1)}$. In the same fashion, since now there is a relation for $f^{(1)}$, we might get a relation for $f^{(2)}$, and so on and so forth.

3.2.3.4 Order equations in original variables

Let us get back to the original variables from the equations above. Taking Eq.127, we have:

$$\begin{aligned}-f_i^{(1)}&=\tau_D\left(\frac{\partial}{\partial t_{D,0}}+C_{i\alpha}\frac{\partial}{\partial \chi_\alpha}\right)f_i^{(0)}\\ \Rightarrow-\varepsilon f_i^{(1)}&=\tau\left(\frac{\partial}{\partial t_0}+c_{i\alpha}\frac{\partial}{\partial x_\alpha}\right)f_i^{(0)}.\end{aligned} \tag{129}$$

We will apply the same procedure with eq. (128), so:

$$\begin{aligned}-f_i^{(2)}&=\left(\tau_D-\frac{1}{2}\Delta t_D\right)\left(\frac{\partial}{\partial t_{D,0}}+C_{i\alpha}\frac{\partial}{\partial \chi_\alpha}\right)f_i^{(1)}+\tau_D\frac{\partial}{\partial t_{D,1}}f_i^{(0)}\\ \Rightarrow-\varepsilon f_i^{(2)}&=\left(\tau-\frac{1}{2}\Delta t\right)\left(\frac{\partial}{\partial t_0}+c_{i\alpha}\frac{\partial}{\partial x_\alpha}\right)f_i^{(1)}+\tau\frac{\partial}{\partial t_1}f_i^{(0)}.\end{aligned} \tag{130}$$

Summing over index i on eqs. 129 and 130 we have:

$$\frac{\partial\rho}{\partial t_0}+\frac{\partial\rho u_\alpha}{\partial x_\alpha}=0, \tag{131}$$

and

$$\frac{\partial\rho}{\partial t_1}=0. \tag{132}$$

Now using the temporal derivative recombination, like

$$\frac{\partial\rho}{\partial t}=\frac{\partial\rho}{\partial t_0}+\varepsilon\frac{\partial\rho}{\partial t_1}, \tag{133}$$

we have:

$$\frac{\partial \rho}{\partial t} + \frac{\partial \rho u_\alpha}{\partial x_\alpha} = 0, \tag{134}$$

which is exactly the conservation of mass up to second order in the Knudsen expansion.

Multiplying eq. 129 by $c_{i\beta}$ and summing over index i on we have:

$$\frac{\partial \rho u_\beta}{\partial t_0} + \frac{\partial \Pi^{(0)}_{\alpha\beta}}{\partial x_\alpha} = 0, \tag{135}$$

where

$$\Pi^{(0)}_{\alpha\beta} = \sum_i f_i^{(0)} c_{i\alpha} c_{i\beta}. \tag{136}$$

The last equation is also equivalent to the second order moment for the equilibrium distribution, already evaluated, and it reads:

$$\begin{aligned} \Pi^{(0)}_{\alpha\beta} &= \sum_i f_i^{(eq)} c_{i\alpha} c_{i\beta} = \\ &= \rho u_\alpha u_\beta + \frac{\rho}{a_s^2}\delta_{\alpha\beta}, \end{aligned} \tag{137}$$

since $c_{i\alpha}c_{i\beta}$ can be written using the second order Hermite polynomial present in Eq.25 as:

$$c_{i\alpha}c_{i\beta} = \mathscr{H}^{(2)}_{\alpha\beta,i} + \frac{\delta_{\alpha\beta}}{a_s^2}. \tag{138}$$

then:

$$\begin{aligned} &\frac{\partial \rho u_\beta}{\partial t_0} + \frac{\partial}{\partial x_\alpha}\left(\rho u_\alpha u_\beta\right) + \frac{\partial}{\partial x_\alpha}\left(\frac{\rho}{a_s^2}\delta_{\alpha\beta}\right) = 0 \\ \Rightarrow &\frac{\partial \rho u_\beta}{\partial t_0} + \frac{\partial}{\partial x_\alpha}\left(\rho u_\alpha u_\beta\right) = -\frac{\partial}{\partial x_\alpha}\left(\frac{\rho}{a_s^2}\delta_{\alpha\beta}\right) = \\ &\qquad = -\frac{\partial}{\partial x_\beta}\left(\frac{\rho}{a_s^2}\right), \end{aligned} \tag{139}$$

so, we need expressions for $\partial \rho / \partial t_0$ and $\partial u_\alpha / \partial t_0$.

From the mass conservation we have:

$$\frac{\partial \rho}{\partial t_0} = -\frac{\partial \rho u_\alpha}{\partial x_\alpha}, \tag{140}$$

which can be readily used to simplify, the second and the last terms on the right hand side of the equation to give:

$$\begin{aligned} -\varepsilon \Pi^{(1)}_{\alpha\beta} &= \tau\left(\frac{\partial}{\partial t_0}\left(\rho u_\alpha u_\beta\right) + \frac{1}{a_s^2}\left(\rho \frac{\partial u_\alpha}{\partial x_\beta} + u_\alpha \frac{\partial \rho}{\partial x_\beta} + \rho \frac{\partial u_\beta}{\partial x_\alpha} + u_\beta \frac{\partial \rho}{\partial x_\alpha}\right)\right) \\ &= \tau\left(\frac{\partial}{\partial t_0}\left(\rho u_\alpha u_\beta\right) + \frac{1}{a_s^2}\left(\rho \frac{\partial u_\alpha}{\partial x_\beta} + \rho \frac{\partial u_\beta}{\partial x_\alpha}\right) + \frac{1}{a_s^2}\left(u_\alpha \frac{\partial \rho}{\partial x_\beta} + u_\beta \frac{\partial \rho}{\partial x_\alpha}\right)\right) \\ &= \tau\left(\frac{\partial}{\partial t_0}\left(\rho u_\alpha u_\beta\right) + \frac{\rho}{a_s^2}2S_{\alpha\beta} + \frac{1}{a_s^2}\left(u_\alpha \frac{\partial \rho}{\partial x_\beta} + u_\beta \frac{\partial \rho}{\partial x_\alpha}\right)\right), \end{aligned} \tag{141}$$

where the strain rate tensor is defined as Eq.39 which then gives:

$$-\varepsilon\Pi^{(1)}_{\alpha\beta} = \tau\left(2\frac{\rho}{a_s^2}S_{\alpha\beta} - \frac{\partial}{\partial x_\gamma}\left(\rho u_\alpha u_\beta u_\gamma\right)\right). \tag{142}$$

This third order term in the velocity is negligible, since the lattice macroscopic velocity u is usually much smaller than one.

$$-\varepsilon\Pi^{(1)}_{\alpha\beta} = 2\tau\frac{\rho}{a_s^2}.S_{\alpha\beta}. \tag{143}$$

Now, we can evaluate:

$$\begin{aligned}
\sum_i\left(f_i^{(eq)} - f_i\right)c_{i\alpha}c_{i\beta} &= -\varepsilon\sum_i f_i^{(1)}c_{i\alpha}c_{i\beta} = \\
\sum_i\left(f_i^{(eq)} - f_i\right)\left(c_{i\alpha}c_{i\beta} - \frac{\delta_{\alpha\beta}}{a_s^2}\right) &= -\varepsilon\Pi^{(1)}_{\alpha\beta} = \\
\rho u_\alpha u_\beta - \rho m^{(2)}_{\alpha\beta} &= 2\tau\frac{\rho}{a_s^2}S_{\alpha\beta} = \\
u_\alpha u_\beta - m^{(2)}_{\alpha\beta} &= \frac{2\tau}{a_s^2}S_{\alpha\beta} \Rightarrow \\
\Rightarrow S_{\alpha\beta} &= \frac{a_s^2}{2\tau}\left(u_\alpha u_\beta - m^{(2)}_{\alpha\beta}\right).
\end{aligned} \tag{144}$$

This means we can evaluate the strain rate tensor locally during a simulation.

$$\begin{aligned}
\tau\frac{\partial\rho u_\beta}{\partial t_1} + \left(\tau - \frac{1}{2}\Delta t\right)\frac{\partial}{\partial x_\alpha}\Pi^{(1)}_{\alpha\beta} &= 0, \\
\frac{\partial\rho u_\beta}{\partial t_1} &= -\left(\tau - \frac{1}{2}\Delta t\right)\frac{\partial}{\partial x_\alpha}\frac{\Pi^{(1)}_{\alpha\beta}}{\tau}.
\end{aligned} \tag{145}$$

since we have:

$$\frac{\partial\rho u_\beta}{\partial t} = \frac{\partial\rho u_\beta}{\partial t_0} + \varepsilon\frac{\partial\rho u_\beta}{\partial t_1}, \tag{146}$$

then:

$$\frac{\partial\rho u_\beta}{\partial t} + \frac{\partial}{\partial x_\alpha}\left(\rho u_\alpha u_\beta\right) = -\frac{\partial p}{\partial x_\beta} + \frac{\partial}{\partial x_\alpha}\left(\frac{\rho}{a_s^2}\left(\tau - \frac{1}{2}\Delta t\right)\left(\frac{\partial u_\alpha}{\partial x_\beta} + \frac{\partial u_\beta}{\partial x_\alpha}\right)\right). \tag{147}$$

If we identify the kinematic viscosity ν and the dynamic viscosity, μ as:

$$\begin{aligned}
\nu &= \frac{1}{a_s^2}\left(\tau - \frac{1}{2}\Delta t\right), \\
\mu &= \rho\nu,
\end{aligned} \tag{148}$$

then:

$$\frac{\partial\rho u_\beta}{\partial t} + \frac{\partial}{\partial x_\alpha}\left(\rho u_\alpha u_\beta\right) = -\frac{\partial p}{\partial x_\beta} + \frac{\partial}{\partial x_\alpha}\left(\mu\left(\frac{\partial u_\alpha}{\partial x_\beta} + \frac{\partial u_\beta}{\partial x_\alpha}\right)\right), \tag{149}$$

and if we compare with the Navier-Stokes equation with the dynamic viscosity μ and bulk viscosity μ_b :

$$\begin{aligned}\frac{\partial \rho u_\beta}{\partial t}+\frac{\partial}{\partial x_\alpha}\left(\rho u_\alpha u_\beta\right) &= -\frac{\partial p}{\partial x_\beta}+\frac{\partial}{\partial x_\alpha}\left(\mu\left(\frac{\partial u_\alpha}{\partial x_\beta}+\frac{\partial u_\beta}{\partial x_\alpha}\right)+\left(\mu_b-\frac{2}{D}\mu\right)\frac{\partial u_\gamma}{\partial x_\gamma}\delta_{\alpha\beta}\right)= \\ &= -\frac{\partial p}{\partial x_\beta}+\frac{\partial}{\partial x_\alpha}\left(\mu\left(\frac{\partial u_\alpha}{\partial x_\beta}+\frac{\partial u_\beta}{\partial x_\alpha}-\frac{2}{D}\frac{\partial u_\gamma}{\partial x_\gamma}\delta_{\alpha\beta}\right)\right)+\frac{\partial}{\partial x_\beta}\left(\mu_b\frac{\partial u_\gamma}{\partial x_\gamma}\right),\end{aligned} \tag{150}$$

we have

$$\begin{aligned}\mu_b &= \frac{2}{D}\mu = \\ &= \frac{2}{D}\rho\nu = \\ &= \frac{2\rho}{a_s^2 D}\left(\tau-\frac{1}{2}\Delta t\right).\end{aligned} \tag{151}$$

4 RESULTS

In this chapter, we present the results of simulations to analyze the behavior of the turbulent jet. We focus on validating the boundary conditions adopted in the proposed domain, making comparisons with previous studies that have addressed the same problem, in order to assess the consistency and accuracy of the data obtained.

The parameters used for the simulation in relation to the dimensions were [256, 1028, 256] lattice points in [x, y, z] for a Cartesian coordinate system. For the velocity we considered $U_J = 0.0256\frac{lu}{ts}$ being "lu" = lattice units and "ts" = time step for a $Re = 2000$ with a simulation time of 3 million cycles.

As described by (Pope 2013), it is possible to do some analysis based on Fig.6, which illustrates the radial velocity profiles of the jet. It can be seen that as the axial distance increases, the jet tends to dissipate and spread across the domain. This behavior was also identified in the simulation carried out, whose visualization of the absolute velocity field $U = \sqrt{u_x^2 + u_y^2 + u_z^2}$ is possible using the Paraview software (Fig.22) and allows the regions described above to be verified with the support of Fig.7 In the simulation shown in Fig.22, the potential core region extends to approximately $15D$, marking the start of the development region. The spread of the jet is clearly seen in the transition between the potential core and the development region.

Figure 22 – **Instantaneous velocity field of the simulation of a turbulent jet** $Re = 2000$ $t = 150x10^3$ **for a) D3Q27 grid model and b) D3Q19 grid model.**

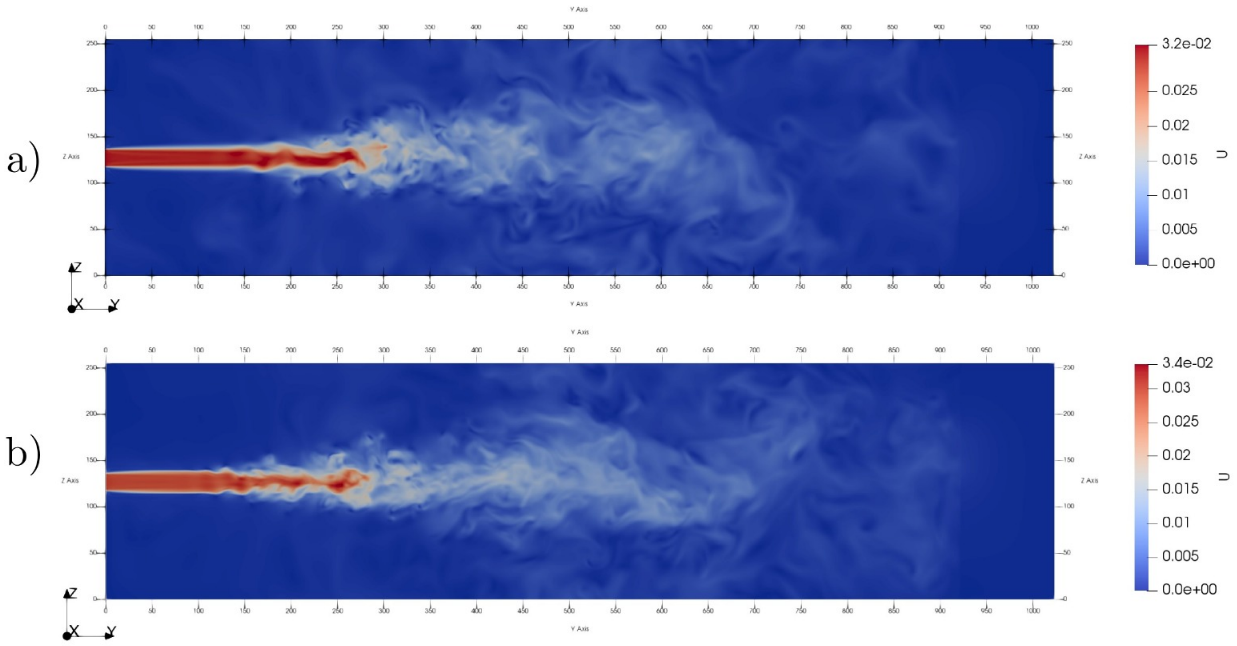

Source: Elaborated by the author (2025).

As the axisymmetric jets have turbulent flow characteristics, it is essential to apply a statistical treatment to the results analyzed.For this reason, a large number of time steps were adopted in order to obtain a sufficiently large sample for calculating the averages.The parameter chosen to monitor the evolution of the simulation was kinetic energy, determined by the following equation:

$$E_c = \frac{1}{2}\left(u_x^2 + u_y^2 + u_z^2\right). \tag{152}$$

As the simulation progresses, the kinetic energy initially grows until it reaches a certain level Fig.23.After this point, an unstable behavior is observed, marked by variations and fluctuations in the kinetic energy values.This phase is identified as the statistically stationary regime, in which the relevant properties are determined by means of time averages. According to (Pope 2013), in turbulent flows, the statistically stationary regime occurs when the averages of the variables remain constant over time, even if these variables continue to oscillate.

Figure 23 – **Evolution of kinetic energy over time steps for a) D3Q27 and b) D3Q19.**

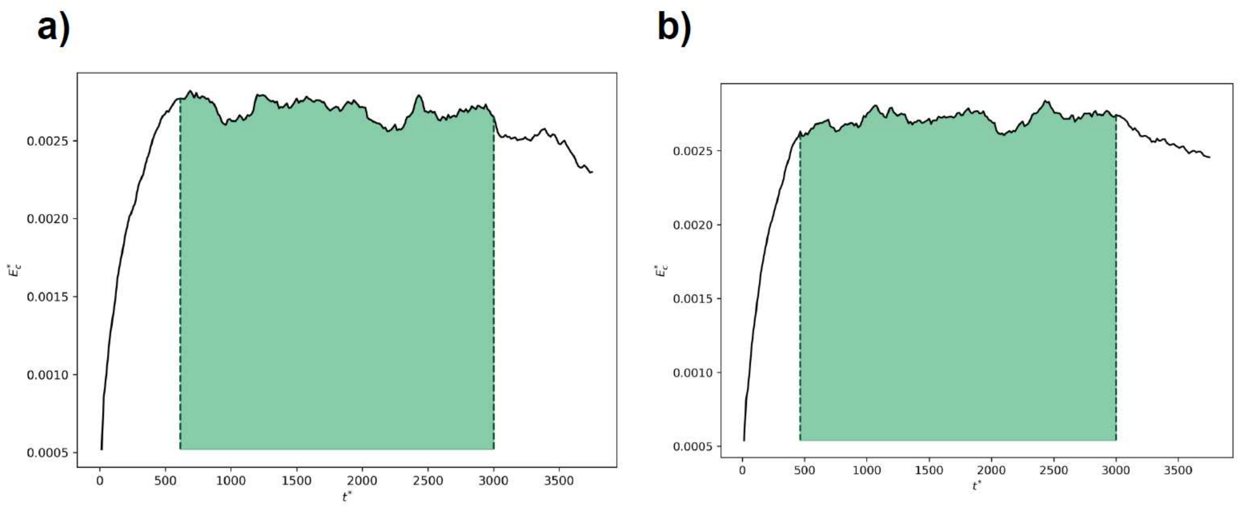

Source: Elaborated by the author (2025).

The dimensionless kinetic energy and time can be described by the following equations:

$$E_c^* = \frac{\sum u^2}{2N_xN_yN_z}. \tag{153}$$

$$t^* = \frac{tU_J}{D}. \tag{154}$$

where t is the instantaneous time step.

Fig.24 and Fig.25 e show the inverse of the axial velocity along the centerline $U_{y,c}$, normalized by the jet inlet velocity U_J. Next to the graph is a visual representation of the center line considered. It can be seen that this value increases along the axial direction, which is related to the spreading of the jet and the consequent reduction in the magnitude of the average velocity in the central region, a behavior that is confirmed by the results obtained.

Figure 24 – **Average velocity profile along the jet centerline for the D3Q27 stencil model.**

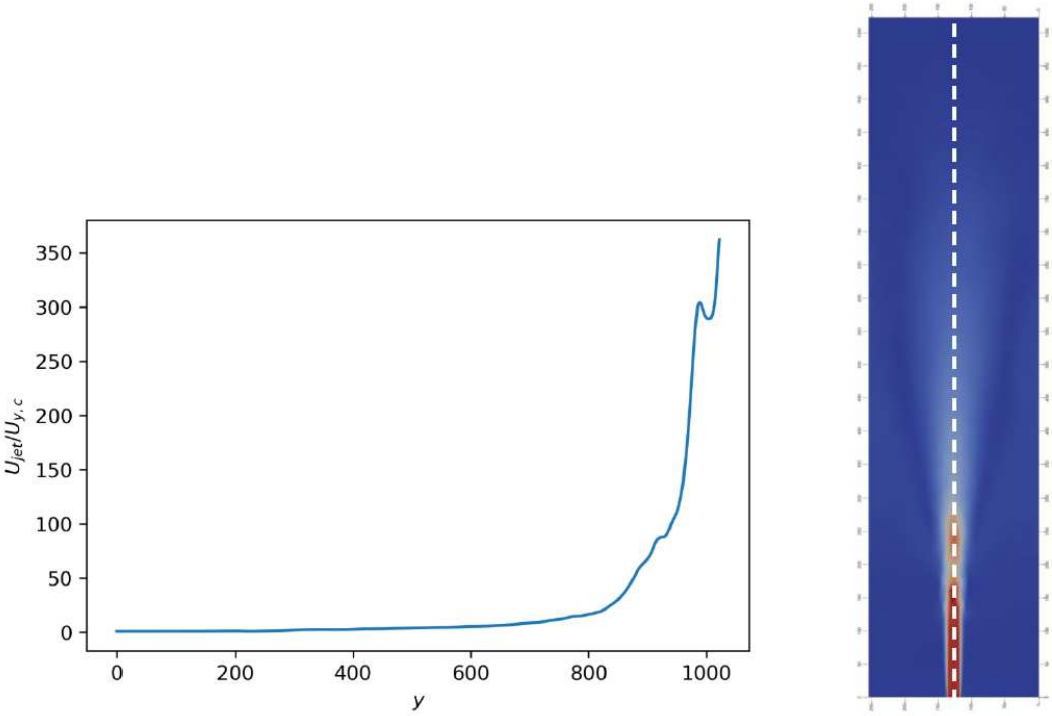

Source: Elaborated by the author (2025).

Figure 25 – **Average velocity profile along the jet centerline for the D3Q19 stencil model.**

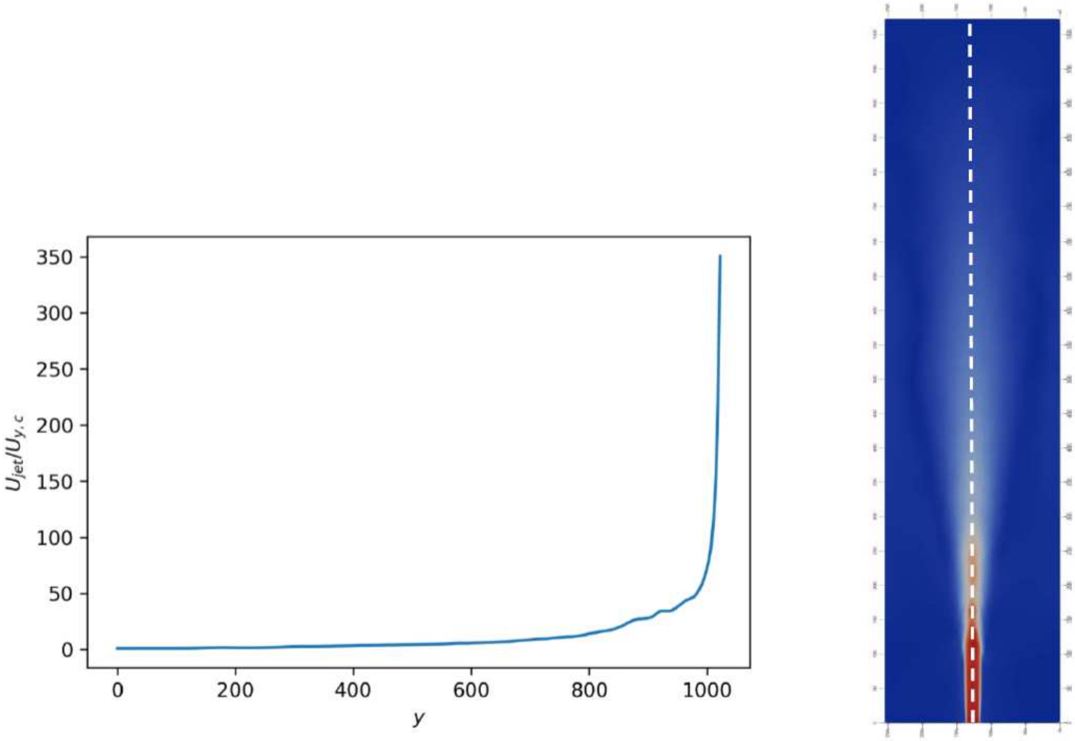

Source: Elaborated by the author (2025).

The development region was delimited between points 300 and 560, corresponding to the intervals from 15D to 28D. Fig.26 and Fig.27 show the ratio $U_J/U_{y,c}$ along the development region as a function of the variable y, normalized by the diameter D. In this range, a new consistency check can be carried out, since the graph must follow the relationship described below:

$$\frac{U_J}{U_{y,c}} = \frac{(y-y_0)}{BD}. \tag{155}$$

Table 1 – **Values obtained for constant B and $(y-y_0)$ for models D3Q19 and D3Q27 compared to the literature.**

Values	D3Q27	D3Q19	(Hussein *et al.* 1994)
B	5.206	5.173	5.8
$(y-y_0)$	4.031	2.495	4.0

Figure 26 – **Illustration of the transition region from the potential core to the development region for a) D3Q27 and b) D3Q19.**

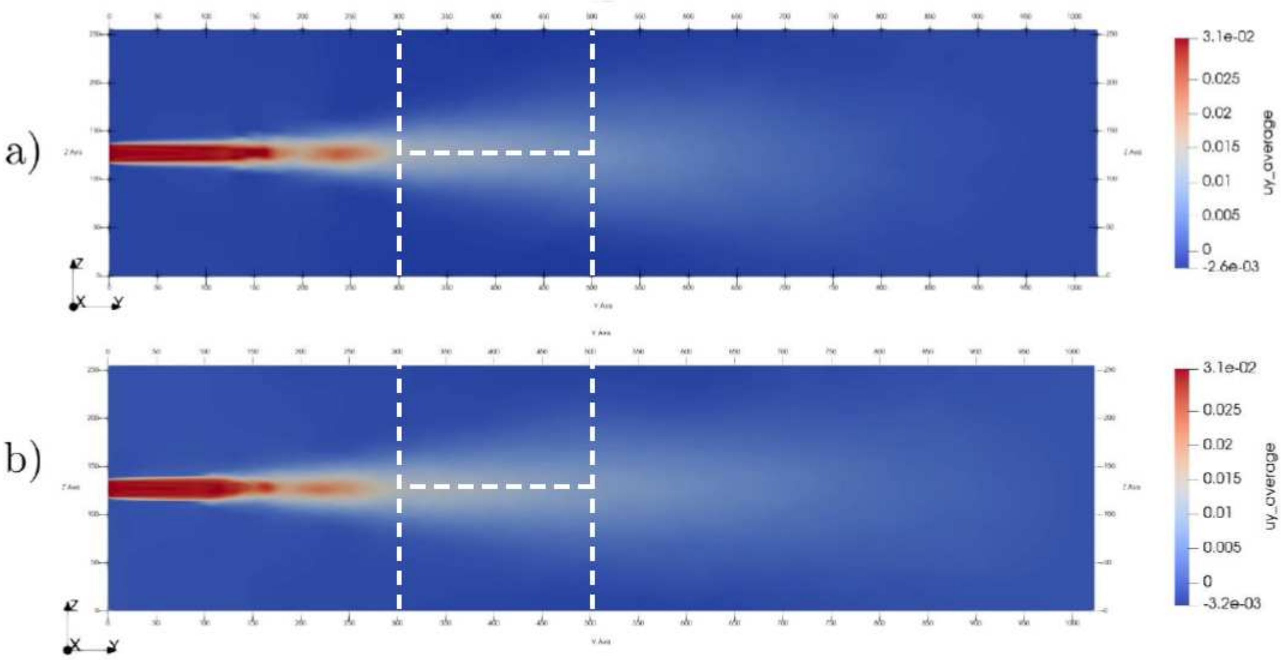

Source: Elaborated by the author (2025).

Figure 27 – **Approximation of the transition region from the potential core to the development region in the graph for a) D3Q27 and b) D3Q19.**

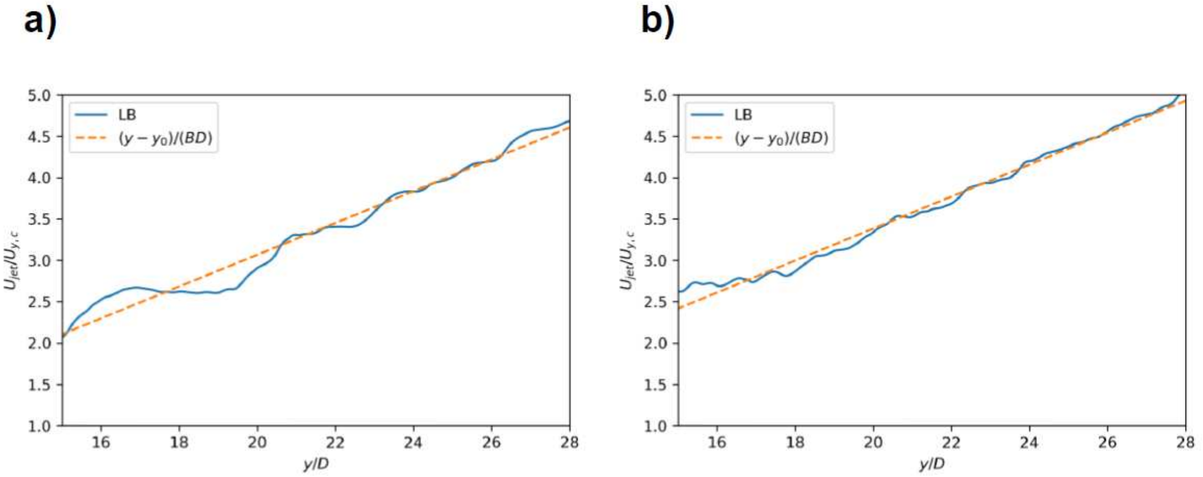

Source: Elaborated by the author (2025).

In the development region, the velocity profiles normalized by the jet inlet velocity are shown in Fig.28 and Fig.29. These profiles were obtained in different sections along the axial axis and then measured along the radius, as illustrated in the representation to the right of the figures.

Figure 28 – **Radial velocity profiles along the axial axis for the D3Q27 stencil model.**

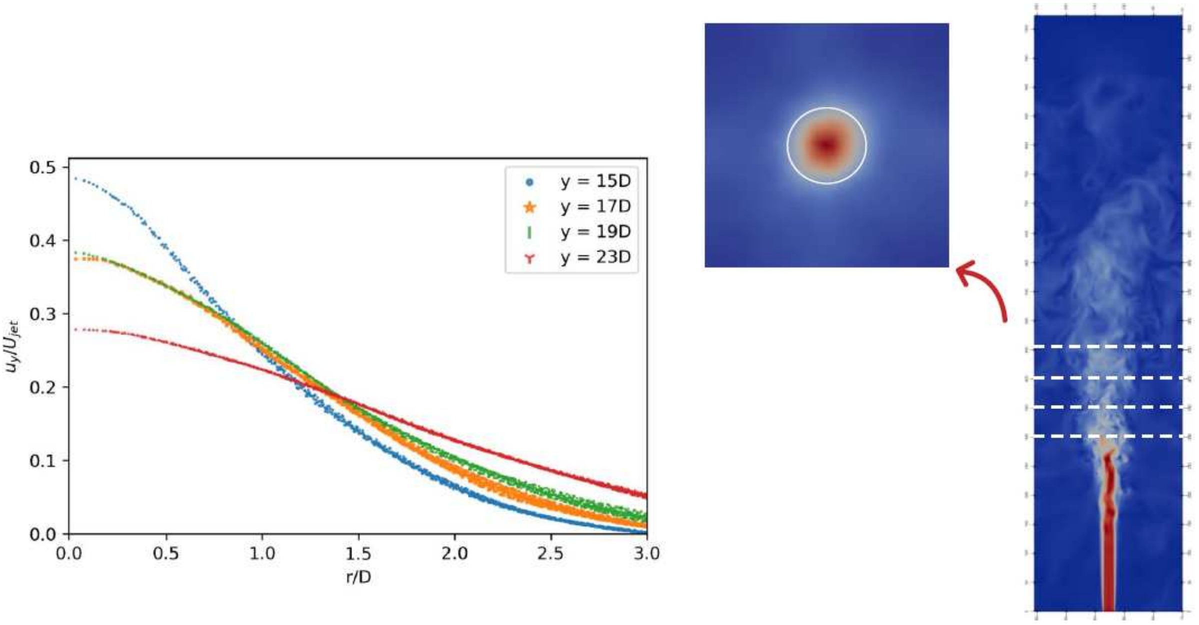

Source: Elaborated by the author (2025).

Figure 29 – **Radial velocity profiles along the axial axis for the D3Q19 stencil model.**

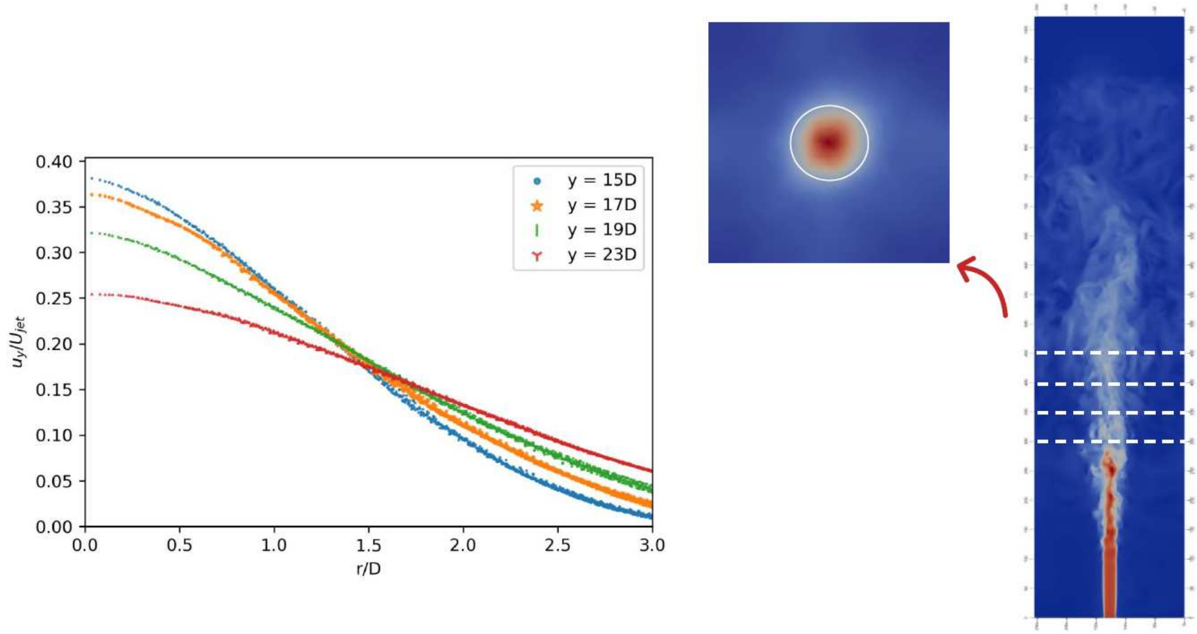

Source: Elaborated by the author (2025).

Although the jet shows spreading followed by decay, the velocity profiles in the development region exhibit a predicted characteristic: self-similarity. This means that, when analyzed along the radius and normalized by the axial distance, the velocities collapse into a single curve, as illustrated in Fig.30 and Fig.31.

Figure 30 – **Self-similar velocity profiles for D3Q27.**

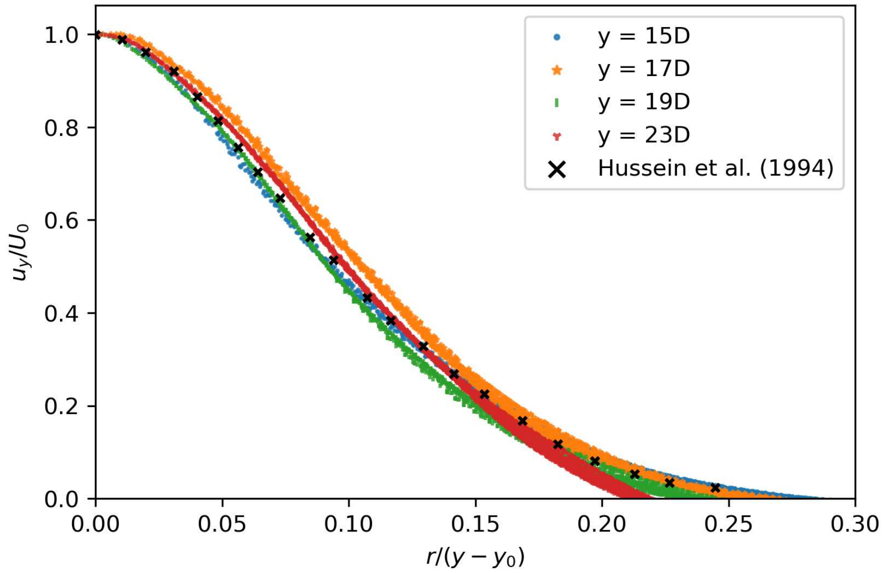

Source: Elaborated by the author (2025).

Figure 31 – **Self-similar velocity profiles for D3Q19.**

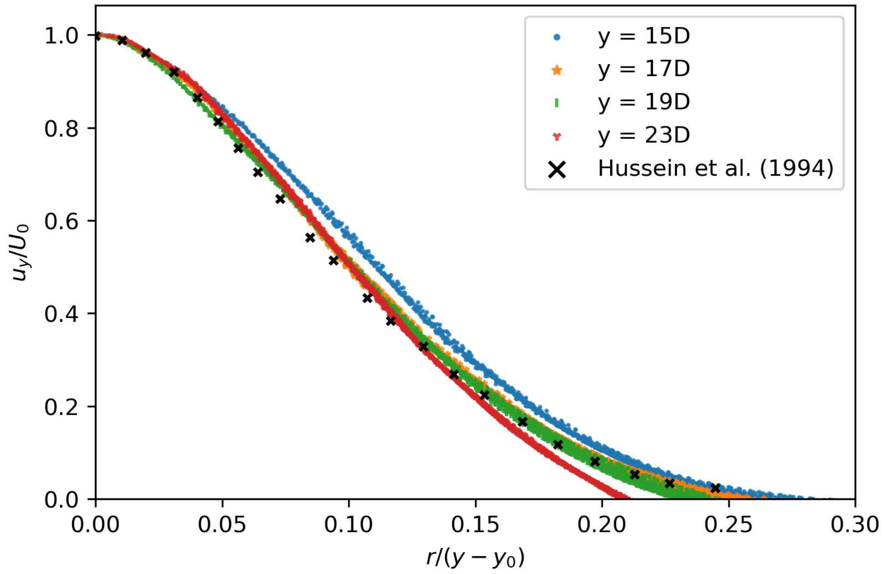

Source: Elaborated by the author (2025).

In Fig.32 and Fig.33 the second moment components of the velocities u_x and u_y for slices 15, 17, 19, 23 scaled along the centerline axis as described by (Hussein *et al.* 1994) are compared with the results in the graph and illustrated in Fig.34. The results showed agreement with the experimental basis at the beginning of the turbulence region for the slices closest to the jet inlet.

Figure 32 – **Axial a) and radial b) RMS values of the fluctuating velocity components for D3Q27**

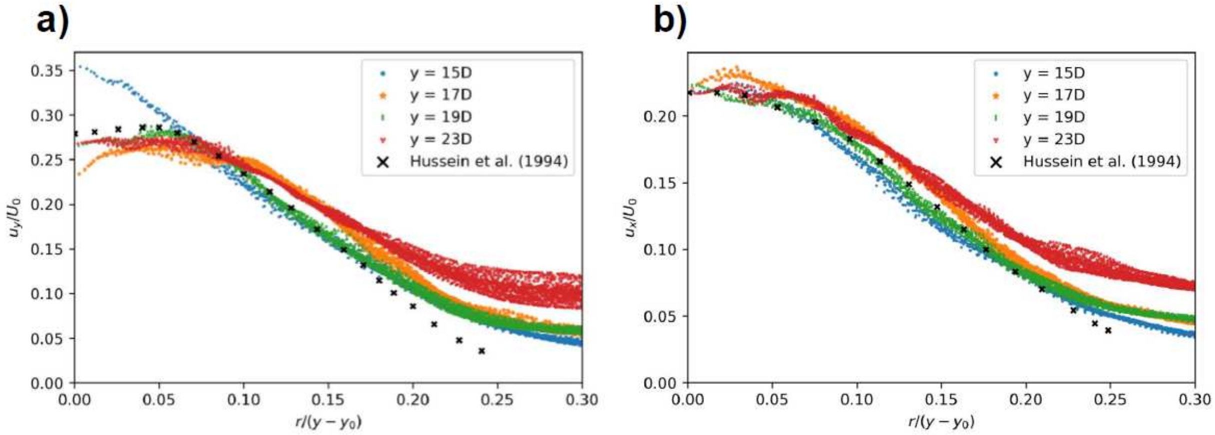

Source: Elaborated by the author (2025).

Figure 33 – **Axial a) and radial b) RMS values of the fluctuating velocity components for D3Q19**

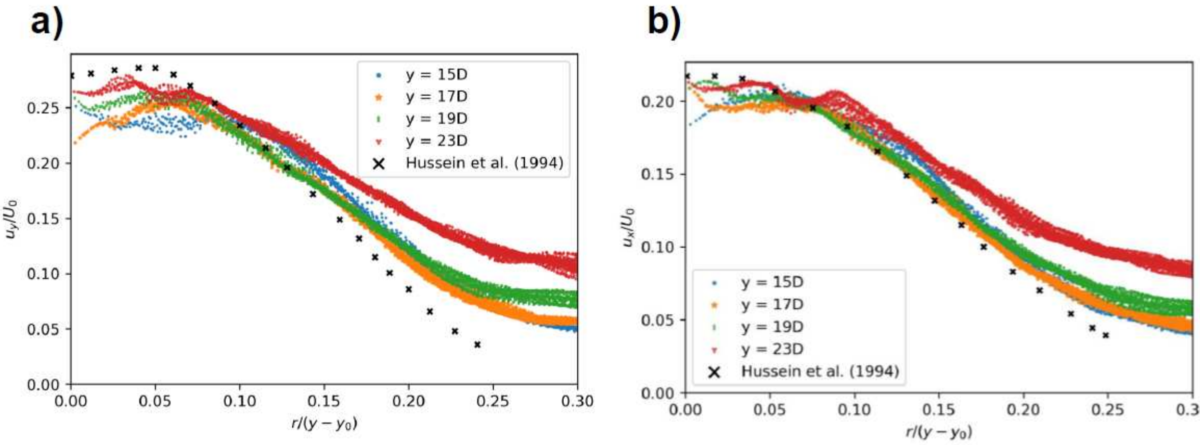

Source: Elaborated by the author (2025).

Figure 34 – **Representation of radial velocity fluctuations along the domain for a) D3Q27 and b) D3Q19**

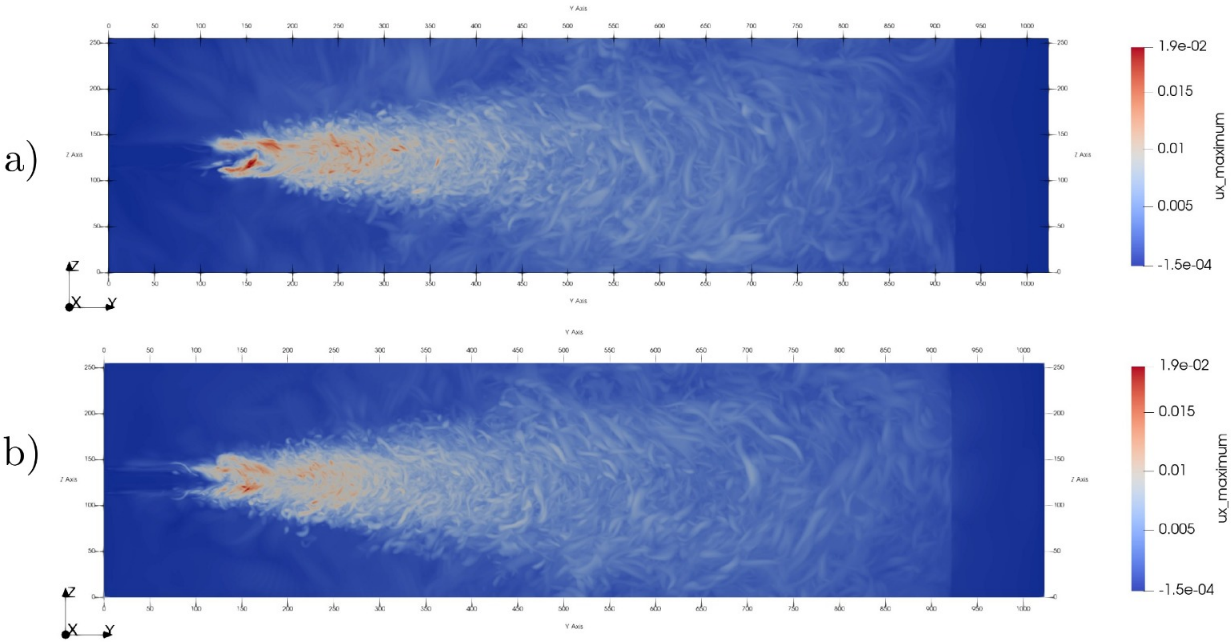

Source: Elaborated by the author (2025).

The solution was developed using code written in CUDA (Compute Unified Device Architecture), a specific language for running on GPUs (Graphics Processing Units), due to its ability to perform calculations significantly faster than on CPUs (Wynters 2011).

The simulations were run on an NVIDIA RTX 4090 GPU, equipped with 24 GB of RAM (Random Access Memory) and 16,384 CUDA cores. The performance obtained during the simulation was measured in MLUPS (Mega Lattice Updates Per Second), which corresponds to the number of points updated per second on the mesh. Performance can be calculated using the following equation:

$$MLUPS = \frac{n_x n_y n_z N_{total}}{10^6 T_{sim}} = 7485, \tag{156}$$

where N_X, N_Y and N_Z represent the total number of points in their respective coordinates, N_{total} the total number of time steps saved and T_{sim} the total simulation time in seconds.

5 CONCLUSION

This work presents a simulation of a single-phase turbulent jet using the lattice Boltzmann method based on moments of order 2^{nd} and periodic boundary conditions on the faces parallel to the jet flow direction, and a refined grid with approximately 6.74 x 10^7 points for a $Re = 2000$ and $U_{Jet} = 0.03$ lu/ts. Two grid models (D3Q27 and D3Q19) were used to simulate the jet, both of which provided results that were consistent with experimental developments, demonstrating high computational performance and fidelity from a physical point of view. For the mathematical model developed, Chapman-Enskog analysis proved that the conditions of conservation of mass and conservation of the amount of movement to second order in the boundary regions and within the domain are respected.

Based on (Hegele.Jr *et al.* 2018), we successfully determined the boundary conditions for the jet inlet, south face and north face using the high-order regularization method. The robust structure of this approach for conserving second-order moments allowed the code developed to operate with a high Re. Features such as the sponge effect and periodic boundary conditions have made it possible to create an environment similar to an infinite domain so that there are no major influences on the limitations of the mesh domain.

The method used made it possible to observe the formation of turbulence with the jet case, which for other methods becomes unfeasible for more refined meshes, as in this case. This is due to the simplicity of the interaction between the mesh points implemented in the method, which speeds up the simulation time without any loss in the physical fidelity of the simulation, so that no resources or pre-developed models are needed to simulate the turbulence.

The simulation developed had a high number of points [256, 256, 1024] for [x, y, z], which requires high processing power to obtain the results. Using a GPU increases the possibility of carrying out simulations with increasingly refined meshes and longer simulation times. Some computational limitations still present for simulation are the need to store the large amount of data generated for the simulations.

COMPLEMENTARY WORKS

Knippenberg, L. D., Czarnobay, V., Hegele Jr., L. A. Simulation of a turbulent jet using the lattice Boltzmann method. In: XII Congresso Nacional de Engenharia Mecânica (CONEM), 2024, Natal, Brasil. https://doi://10.26678/ABCM.CONEM2024.CON24-1188

Knippenberg L. D., Choaire, G. T., Czarnobay, V., Hegele Jr., L. A. Couette flow simulation using lattice Boltzmann method. In: 20th Brazilian Congress of Thermal Sciences and Engineering (ENCIT), 2024, Foz do Iguaçu, Brasil.

Knippenberg L. D., Choaire, G. T., Czarnobay, V., Hegele Jr., L. A. High Reynolds number flow simulation in a square duct using the lattice Boltzmann method. In: 12º Congresso Brasileiro de Pesquisa e Desenvolvimento em Petróleo e Gás (PDPETRO), 2024.

BIBLIOGRAPHY

ANDERSON, Daniel M; MCFADDEN, Geoffrey B; WHEELER, Adam A. Diffuse-interface methods in fluid mechanics. **Annual review of fluid mechanics**, Annual Reviews 4139 El Camino Way, PO Box 10139, Palo Alto, CA 94303-0139, USA, v. 30, n. 1, p. 139–165, 1998.

BATCHELOR, GK; GILL, AE152222. Analysis of the stability of axisymmetric jets. **Journal of fluid mechanics**, Cambridge University Press, v. 14, n. 4, p. 529–551, 1962.

BAZARIN, RLM *et al.* Moments-based method for boundary conditions in the lattice boltzmann framework: A comparative analysis for the lid driven cavity flow. **Computers & Fluids**, Elsevier, v. 230, p. 105142, 2021.

BEAVERS, Gordon S; WILSON, Theodore A. Vortex growth in jets. **Journal of Fluid Mechanics**, Cambridge University Press, v. 44, n. 1, p. 97–112, 1970.

BHATNAGAR, Prabhu Lal; GROSS, Eugene P; KROOK, Max. A model for collision processes in gases. i. small amplitude processes in charged and neutral one-component systems. **Physical review**, APS, v. 94, n. 3, p. 511, 1954.

BRANDVIK, Per Johan *et al.* Reducing oil droplet sizes from a subsea oil and gas release by water jetting a laboratory study performed at different scales. **Marine Pollution Bulletin**, Elsevier, v. 193, p. 115009, 2023.

BRITO, Pedro Paulo de Carvalho *et al.* Método lattice-boltzmann aplicado a aerodinâmica externa. Universidade Federal de Uberlândia, 2017.

ÇENGEL, YA; CIMBALA, JM; TURNER, RH. **“Fundamentals of Fluid Mechanics, SI UNITS (Core Version)**. [S.l.]: Mcgraw Hill Book co., USA, 2018.

CHEN, Yilin *et al.* An efficient framework for particle-fluid interaction using discrete element lattice boltzmann method: Coupling scheme and periodic boundary condition. **Computers & Fluids**, Elsevier, v. 208, p. 104613, 2020.

CORRSIN, Stanley. **Investigation of flow in an axially symmetrical heated jet of air**. [S.l.], 1943.

DAHM, Werner JA; DIMOTAKIS, Paul E. Mixing at large schmidt number in the self-similar far field of turbulent jets. **Journal of Fluid Mechanics**, Cambridge University Press, v. 217, p. 299–330, 1990.

FERRARI, Marco A; FRANCO, Admilson T. The steady and unsteady regimes in a cubic lid-driven cavity with viscoplastic fluid solved with the lattice boltzmann method. **Journal of Non-Newtonian Fluid Mechanics**, Elsevier, p. 105198, 2024.

GRANT, AJ. A numerical model of instability in axisymmetric jets. **Journal of Fluid Mechanics**, Cambridge University Press, v. 66, n. 4, p. 707–724, 1974.

GRANT, AJ; JONES, JM; ROSENFELD, JLJ. Orderly structure and unmixedness in lifted jet diffusion flames. In: ACADEMIC PRESS. **Combustion Institute European Symposium**. [S.l.], 1973. p. 548–552.

HEGELE.JR, LA *et al.* High-reynolds-number turbulent cavity flow using the lattice boltzmann method. **Physical Review E**, APS, v. 98, n. 4, p. 043302, 2018.

HUSSEIN, Hussein J; CAPP, Steven P; GEORGE, William K. Velocity measurements in a high-reynolds-number, momentum-conserving, axisymmetric, turbulent jet. **Journal of Fluid Mechanics**, Cambridge University Press, v. 258, p. 31–75, 1994.

JAMET, Didier. Diffuse interface models in fluid mechanics. **GdR CNRS documentation, see pmc. polytechnique. fr/mp/GDR/docu/Jamet. pdf**, 2001.

KRUGER, Timm. **Lattice Boltzmann Method-Principles and Practice**. [S.l.]: Springer International Publish, 2016.

LI, Wei *et al.* High-order moment-encoded kinetic simulation of turbulent flows. **ACM Transactions on Graphics (TOG)**, ACM New York, NY, USA, v. 42, n. 6, p. 1–13, 2023.

LIPARI, Giordano; STANSBY, Peter K. Review of experimental data on incompressible turbulent round jets. **Flow, turbulence and combustion**, Springer, v. 87, p. 79–114, 2011.

LIST, EJ. Mechanics of turbulent buoyant jets and plumes. In: **Turbulent buoyant jets and plumes**. [S.l.]: Elsevier, 1982. p. 1–68.

MONTESSORI, Andrea *et al.* High-order thread-safe lattice boltzmann model for high performance computing turbulent flow simulations. **Physics of Fluids**, AIP Publishing, v. 36, n. 3, 2024.

PANCHAPAKESAN, Nagangudy R; LUMLEY, John L. Turbulence measurements in axisymmetric jets of air and helium. part 1. air jet. **Journal of Fluid Mechanics**, Cambridge University Press, v. 246, p. 197–223, 1993.

PHILIPPI, Paulo Cesar. **Thermodynamics: From Fundamentals to Multiphase and Multicomponent Systems**. [S.l.]: Springer Nature Switzerland, Imprint: Springer, 2024.

POPE, Stephen B. **Turbulent flows**. [S.l.: s.n.], 2013. v. 12. 2020–2021 p.

PRASAD, Ajay K; KOSEFF, Jeffrey R. Reynolds number and end-wall effects on a lid-driven cavity flow. **Physics of Fluids A: Fluid Dynamics**, AIP, v. 1, n. 2, p. 208–218, 1989.

REICHARDT, H. Über eine neue theorie der freien turbulenz. **ZAMM-Journal of Applied Mathematics and Mechanics/Zeitschrift für Angewandte Mathematik und Mechanik**, Wiley Online Library, v. 21, n. 5, p. 257–264, 1941.

RODI, Wolfgang. A new method of analysing hot-wire signals in highly turbulent flow, and its evaluation in a round jet. **Disa Information**, p. 9–18, 1975.

SHEKHAR, Chandra; NISHINO, Koichi. Turbulence energetics in an axisymmetric impinging jet flow. **Physics of Fluids**, AIP Publishing, v. 31, n. 5, 2019.

SUCCI, Sauro. **The lattice Boltzmann equation: for fluid dynamics and beyond**. [S.l.]: Oxford university press, 2001.

TENNEKES, Hendrik; LUMLEY, John Leask. **A first course in turbulence**. [S.l.]: MIT press, 1972.

VARDHAN, Madhurima *et al.* Moment representation in the lattice boltzmann method on massively parallel hardware. In: **Proceedings of the International Conference for High Performance Computing, Networking, Storage and Analysis**. [S.l.: s.n.], 2019. p. 1–21.

WHITE, Frank M; MAJDALANI, Joseph. **Viscous fluid flow**. [S.l.]: McGraw-Hill New York, 2006. v. 3.

WYGNANSKI, Israel; FIEDLER, Ho. Some measurements in the self-preserving jet. **Journal of Fluid Mechanics**, Cambridge university press, v. 38, n. 3, p. 577–612, 1969.

WYNTERS, Erik. Parallel processing on nvidia graphics processing units using cuda. **Journal of Computing Sciences in Colleges**, Consortium for Computing Sciences in Colleges, v. 26, n. 3, p. 58–66, 2011.

XUE, Xiao; YAO, Hua-Dong; DAVIDSON, Lars. Synthetic turbulence generator for lattice boltzmann method at the interface between rans and les. **Physics of Fluids**, AIP Publishing, v. 34, n. 5, 2022.